

Designing against severe stresses at compound cooling holes of double wall transpiration cooled engine components

Christos G. Skamniotis and Alan C.F. Cocks

Department of Engineering Science, University of Oxford, Parks Road,
Oxford OX7 6DP, UK

ABSTRACT

Advanced thermal protection technology is key for allowing hotter gas turbine cycle temperatures towards minimising fuel consumption and emissions. While effusion holes are essential for reducing heat flux into the structure through the formation of an air cool layer between the hot gas flow and the solid, they can shorten component life due to local stress raising effects. Through Finite Element (FE) analysis, we evaluate the severity of these effects in double wall transpiration cooling (DWTC) systems under thermal loading and identify how mechanical performance can be improved by modifying global and local geometric features. Increasing effusion hole inclination to 60° to the surface normal leads to extreme stress concentration factors (SCFs), which can exceed 5. Eliminating ellipticity in the effusion hole surface is shown to offer enormous performance benefits, by decreasing the SCF by 50%. A narrow spacing between the wall-connecting pedestals implies shorter hole-hole and hole-pedestal distances, which also leads to a reduction of SCFs. Our elastic solutions can be readily used in fatigue life calculations based on Neuber type local strain approaches. They also establish the basis for understanding the response of the new systems under combined thermal-mechanical loading.

Keywords: Effusion/film holes, hole inclination, stress concentration, thermal stresses, double wall transpiration cooling system.

Nomenclature

Abbreviations

FE = finite elements

CFD = computational fluid dynamics

SCF = stress concentration factor

2D = two-dimensional

3D = three-dimensional

MPC = multipoint constraint

DWTC = double wall transpiration cooling

max = maximum

Symbols

Thermal

T_{max} = maximum temperature (K)

T_{min} = minimum temperature (K)

T_0 = reference/room temperature (K)

ΔT = thermal gradient (K/mm)

Structural

R = radius of curvature (mm)

t = wall thickness (mm)

D = diameter (mm)

γ = inclination (degrees)

H = wall spacing/pedestal height (mm)

L = pedestal spacing (mm)

ρ = fillet radius (mm)

ψ = unit cell angle (rad)

ω = wedge angle (degrees)

Material

E = Elastic Modulus (MPa)

ν = Poisson's ratio

α = thermal expansion coefficient (m/m·K)

k = thermal conductivity (W/m·K)

Mechanical

u = displacement (mm)

ϕ = rotation (rad)

N = membrane force per unit length (N/mm)

M = bending moment per unit length (N·mm/mm)

σ = maximum absolute principal (Cauchy) stress (MPa)

σ_j = (Cauchy) stress component (MPa) in j direction

σ_1 = maximum principal stress (MPa)

σ_2 = medium principal stress (MPa)

σ_3 = minimum principal stress (MPa)

Accents – superscripts

$\hat{}$ = quantity normalised over outer hot wall thickness (dimensionless)

$\bar{}$ = dimensionless position or average value

Subscripts

h = outer hot wall property

c = inner cool wall property

O = hole property

ef = effusion hole property

imp = impingement hole property

P = pedestal property

f = fillet property

θ = circumferential axis/direction of cylindrical wall

z = longitudinal axis/direction of cylindrical wall

r = radial axis/direction of cylindrical wall

ξ = relative circumferential position wall

ζ = relative axial position of cylindrical wall

x = horizontal (in-plane) axis/direction of flat plate

y = horizontal (in-plane) axis/direction of flat plate

z = vertical (out-of-plane) axis/direction of flat plate

1. Introduction

Temperature is a limiting factor in gas turbine, hypersonic flight and power generation. Advances in nickel superalloys and thermal barrier coatings have served to increase the acceptable operating temperatures of hot fluids near structural components [2, 3], addressing both the efficiency and structural integrity demands of high temperature applications [4]. The improvement of cooling strategies has contributed far more significantly over the last fifty years, such that, today, solids can be exposed to temperatures beyond their engineering limits. This creates enormous opportunities, particularly in gas turbines where increasing core gas temperatures increases their efficiency and specific power output [5], promising less fuel consumption and less environmentally damaging emissions [6, 7].

Such achievements necessitate the reduction of heat flux from the hot gas into the solid. This is best addressed by using porous solid surfaces with effusion/film holes in order to eject cool air towards the hot gas flow to form a protective cool buffer layer [8-11]. Additional features are introduced to take further advantage of the coolant by also promoting internal impingement cooling [12, 13]. The amalgamation of the above effusion-impingement functions has led to the double wall transpiration cooling (DWTC) concept in Fig 1a, also represented by the repeating unit cell in Figs 1b-b'. This concept is widely recognised as state-of-the-art in terms of cooling effectiveness and convective efficiency [3, 4, 12, 14].

Despite these benefits, structural integrity has received limited attention [14, 15] which has delayed the implementation of DWTCs [10, 14, 16-18]. Major concerns relate to the presence of weak points, such as holes and wall-connecting pedestal fillets (see Fig 1b), which cause stress raising effects that compromise integrity [19-22]. The coupling of two walls experiencing largely different temperatures is also suggested to cause severe thermal stresses compared to conventional single wall components [14, 17, 23-26].

Stress analysis of DWTC systems has only been reported by Murray et al [14], Elmukashfi et al [15] and recently by the authors [27, 28]. In the latest study [28] the authors demonstrated the high sensitivity of thermal stresses with respect to the kinematic constraints of the system [27]. Tensile stresses at pedestal fillets were shown to increase sharply if pedestal diameter is reduced below a critical value [28].

A major omission in all these previous studies was the effect of holes on the resulting stress field. It was assumed that holes only increase locally the nominal thermal stresses by a stress concentration factor (SCF) and it was therefore argued that one way of minimising hole stresses is to minimise the nominal stresses acting at the corresponding hole locations, through global geometric modifications of the DWTC system.

The present paper assesses the validity of the above argument in realistic DWTC geometries and explores in detail the parameters that influence the SCF. The latter provides answers to key design questions, such as whether hole stresses can be effectively minimised by reducing the SCF through a combination of local modifications, i.e. by altering hole shape-size, and global modifications, i.e. by altering hole-hole and hole-pedestal distances. These aspects are explored here by a systematic approach in which the hole stresses are given by the superposition of: (a) the nominal thermal stress field in the absence of holes; (b) the stress concentration factor (SCF) associated with an isolated hole in a plate, i.e. independent of hole-hole and hole-pedestal interactions; and (c) the perturbation of SCF caused by interactions. Major features of the approach adopted here are:

- It adopts temperature, geometric and material idealisations in order to provide a physical interpretation of the stress field and the manner in which peak stresses are influenced by global and local geometric features, such as wall thickness and spacing, as well as by the boundary and loading conditions. This provides important information about how the stresses are changed by a

change of geometry, particularly in the vicinity of holes, which is important in design and which cannot be obtained from detailed one-off finite element solutions for specific, non-idealised conditions and geometries.

- It decomposes, for the first time, the individual effects of ellipticity and inclination on the SCF in oblique holes and also explores in detail the roles of: (a) the nominal stress distribution through the thickness, (b) the biaxial (in-plane) stress ratio, and (c) the hole fillet; although these three aspects have been studied for transverse circular [29, 30] and transverse elliptical holes [31-34], very little is known for oblique holes [35-42].

The detailed understanding of the individual parameters that influence the SCF developed here, creates possibilities for using holes with large inclinations (for high film effectiveness [10, 17, 43, 44]) and simultaneously with shapes that are adjusted to the nominal stress field characteristics to give the minimum possible SCF; advances in new manufacturing methods, e.g. additive manufacturing [45], will enable the implementation of such ideas. The results of the present paper also: (a) indicate the pathways for modifying geometric features towards optimal mechanical performance; (b) reduce the range of geometries that needs to be analysed in the plasticity-creep range, including complex temperature fields and cyclic thermomechanical loading conditions; (c) provide the thermoelastic stress range at critical locations, which can be associated with shakedown and ratcheting limits [46-50] and can also be readily used in fatigue life calculations based on Neuber type local strain approaches [51-53]; and (d) establish a strong foundation for exploring more detailed phenomena related to the directional [54, 55] and temperature dependence [56] of material properties, as well as evaluating crystallographic slip failure mechanisms [57, 58].

In Section 2 we describe our FE modelling methodology along with the structural constraints as well as our temperature field and geometric assumptions. In Section 3 we present stress-geometry relationships for double walls in the absence of holes, in Section 4 we report SCF solutions for isolated holes in large flat plates and in Section 5 we present our full solutions for the DWTC system in the presence of holes.

system idealisation

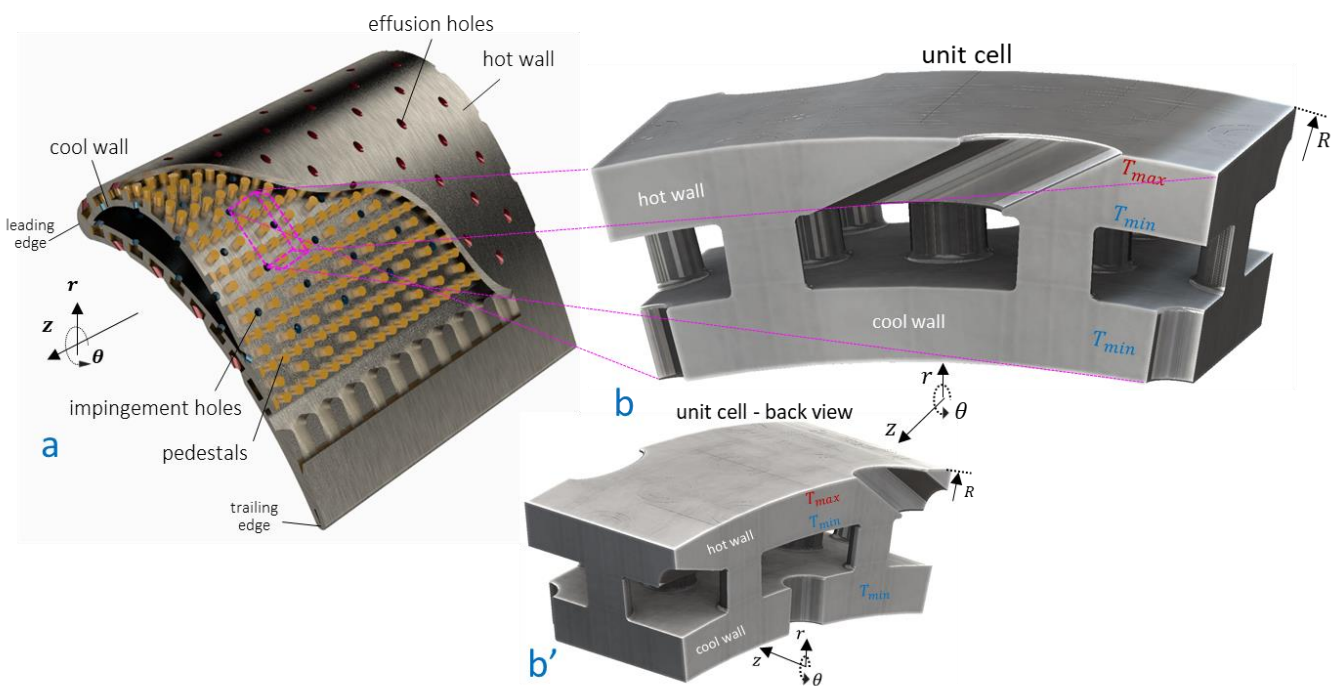


Figure 1. Illustration of a typical double wall transpiration cooling system. Images show: (a) system implemented in a gas turbine blade – image reproduced from [1]; (b) periodically repeating unit cell of the system in Fig 1(a) with idealised constant external radius of curvature, R , and maximum-minimum metal temperatures; (b') back view of the unit cell in Fig 1b.

2. Methodology

2.1 Temperature field

We adopt the temperature field idealisation used in [15, 28]. This involves a uniform temperature gradient, $\Delta T = (T_{max} - T_{min})/t_h$, across the thickness of the outer hot wall, t_h (see Fig 1b), generated by a temperature, T_{max} , at the hot outer surface of the hot wall and temperature, T_{min} , in the inner cool surfaces of the system. Our recent study [28] supports this idealisation strategy for developing an understanding of the effect of kinematic constraint and various geometric features on the stress state, since the temperature field is only described by the single parameter, ΔT , and therefore thermal stresses scale with $E\alpha\Delta T$ (E is the Young's Modulus and α is the thermal expansion coefficient). The idealisation is based on solutions for the steady state temperature field obtained in a number of solid-fluid heat transfer studies [14, 59, 60] through conjugate Computational Fluid Dynamics (CFD) and heat conduction simulations. Elmukashfi et al. [15] demonstrated that, despite these simulations showing that T_{max} and T_{min} vary along the outer hot wall surface and throughout the internal surfaces, respectively, that the assumption of constant ΔT throughout the hot wall induces a 10% maximum error in the hot wall nominal stresses. This implies that the stress state in the vicinity of effusion holes is dictated by the global features of the temperature field, rather than the temperature perturbations near the holes. A concurrent study [61] further supports this argument based on results for the system of Fig 1b, obtained through a series of CFD-heat transfer-FE stress analyses. These studies allow us to assume that the stress state in the vicinity of holes is not influenced by the different temperature perturbations that would in practice occur when the hole shape-size characteristics are modified. We anticipate, however, that the effusion hole shape-size will influence the average temperature in the outer hot wall surface, and therefore the average value of ΔT , and thus the scaling factor $E\alpha\Delta T$ of the nominal stress field. For this reason, throughout the study our stress results are normalised by $E\alpha\Delta T$.

2.2 Geometry

Geometric idealisations are also adopted according to our recent study [28]. These mainly involve the assumption of a constant curvature in the two walls, giving rise to the unit cell in Figs 1b-b', which represents the concentric double cylindrical walls connected with pedestals, with some pedestals being periodically absent to accommodate the effusion and impingement holes; consider the origin of the cylindrical system, $r\theta z$, in Figs 1b-b' (and Figs 2a, 2c) to be at the centre of the external geometric curvature, $1/R$. We have shown that effects arising by a variable wall curvature (Fig 1a) are of local character [28] and may become significant only at a small curvatures, i.e. $R/t_h < 20$, which are relevant to the leading edge of the blade in Fig 1a. Here we will use a fixed ratio of $R/t_h = 20$ (see Fig 1b).

Fig 1b involves global features dictating the nominal thermal stress field and local features that control locally the SCF at holes and pedestals. Global features are denoted in the FE model of Fig 2a which is part of the unit cell in Fig 1b, and include the hot (outer) wall thickness, t_h , the cool (inner) wall thickness, t_c , the wall spacing (pedestal height), H , as well as the pedestal spacing, L_θ and L_z in the θ , and z directions. Local features are denoted within the FE model of Fig 2c, and include the pedestal diameter, D_p , the effusion and impingement hole diameters, $D_{O_{ef}}$, $D_{O_{imp}}$, the pedestal-wall fillet radius, ρ_{p_f} , the effusion and impingement hole fillet radii, $\rho_{O_{ef}}$, $\rho_{O_{imp}}$, as well as the effusion hole inclination, γ . We will refer to different geometries by normalising all the parameters with

respect to the fixed hot wall thickness, $t_h = 1$ mm i.e. by the ratios, $\hat{R} = R/t_h$, $\hat{t}_c = t_c/t_h$, $\hat{H} = H/t_h$, $\hat{L}_\theta = L_\theta/t_h$, $\hat{L}_z = L_z/t_h$, $\hat{D}_p = D_p/t_h$, $\hat{D}_{O_{ef}} = D_{O_{ef}}/t_h$, $\hat{D}_{O_{imp}} = D_{O_{imp}}/t_h$, $\hat{\rho}_{P_f} = \rho_{P_f}/t_h$, $\hat{\rho}_{O_{ef}} = \rho_{O_{ef}}/t_h$, $\hat{\rho}_{O_{imp}} = \rho_{O_{imp}}/t_h$. Pedestal spacing, L_θ , refers to the arc-length between pedestals that accommodates the effusion/impingement holes and it is measured at the inner surface of the hot wall (see Fig 2a), defining the angle, $\psi = (\hat{L}_\theta/2 + \hat{D}_p/2)/(\hat{R} - 1)$, as denoted in Figs 2a, 2c. The centre of the intersection/rim of the effusion hole with the inner surface of the hot wall (denoted as O in Fig 2c) is always located at the centre of the pedestal spacing L_θ and L_z ; the impingement hole is located in the same manner.

2.3 FE modelling

2.3.1 Numerical strategy

Our FE modelling strategy is illustrated in Figs 2a-c. The FE model in Fig 2a uses the 1/8 fraction of the unit cell in Fig 1b to provide thermal stress solutions in the absence of holes. This model (Fig 2a) has been previously described in [28]. Therefore, detailed descriptions will be provided here only for the FE models in Figs 2b-c where holes are present.

We use the nominal stress field solutions obtained for the hot wall in Fig 2a, as load boundary conditions in the hole-flat plate model in Figs 2b-b', i.e. membrane forces and bending moments in the two principal directions, x and y ; in this way, we predict effusion hole peak stresses in the absence of hole-pedestal interaction. We consistently use a large enough plate of 10 x 10 x 1 mm (length x width x thickness) to ensure that the SCF is not influenced by edge effects, i.e. are consistent with the assumption of infinite plate. Finally, we simulate the response of the DWTC system in the presence of holes through the FE model of Fig 2c, which uses 1/3rd of the actual unit cell in Fig 1b, on the basis that larger cells practically lead to the same results (to be discussed in Section 2.3.2).

An implicit steady-state coupled temperature-displacement analysis is performed within the commercial FE code ABAQUS [62], based on the material parameters: $E = 120000$ MPa, $\nu = 0.3$, $\alpha = 1.2 \cdot 10^{-5}$ m/m·K [28]. Arbitrary values of $T_{max} = 1000$ K and $T_{min} = 300$ K, are used for the temperatures applied across the surfaces denoted in Figs 2a,b.

2.3.2 Structural constraints - boundary conditions

In Fig 2b we apply symmetry boundary conditions i.e. $u_x = 0$ and $u_y = 0$ (u -displacement) at two faces of the plate, perpendicular to each other, while surface tractions are applied normal to the surface on the opposite faces, i.e. external membrane forces and bending moments; $u_z = 0$ is also imposed at one corner node of the plate. For inclined holes, such as the one shown in Fig 2b, we model half of the actual geometry, whereas for transverse circular/elliptical holes the domain is reduced to a quarter.

The boundary conditions in Fig 2a,b were previously reported in [28], and are briefly described here. $u_\theta = 0$ is applied at the symmetry planes, $\bar{\theta} = 0$ and $\bar{\theta} = 1$ and $u_z = 0$ is applied at plane, $\bar{z} = 1$. For plane, $\bar{z} = 0$, two constraint cases are used, denoted as A and B. In case A the walls cannot rotate about the θ axis i.e. $\varphi_{\theta_h} = \varphi_{\theta_c} = 0$, and thus all the nodes at $\bar{z} = 0$ translate by an equal amount, u_z . In case B the condition $\varphi_{\theta_h} = \varphi_{\theta_c} \neq 0$ prevails, implying that the z extensions of two walls are proportional, as the plane, $\bar{z} = 0$, must deform into a conical surface. This kinematic condition is numerically enforced through the ABAQUS MPC subroutine [28].

FE modelling

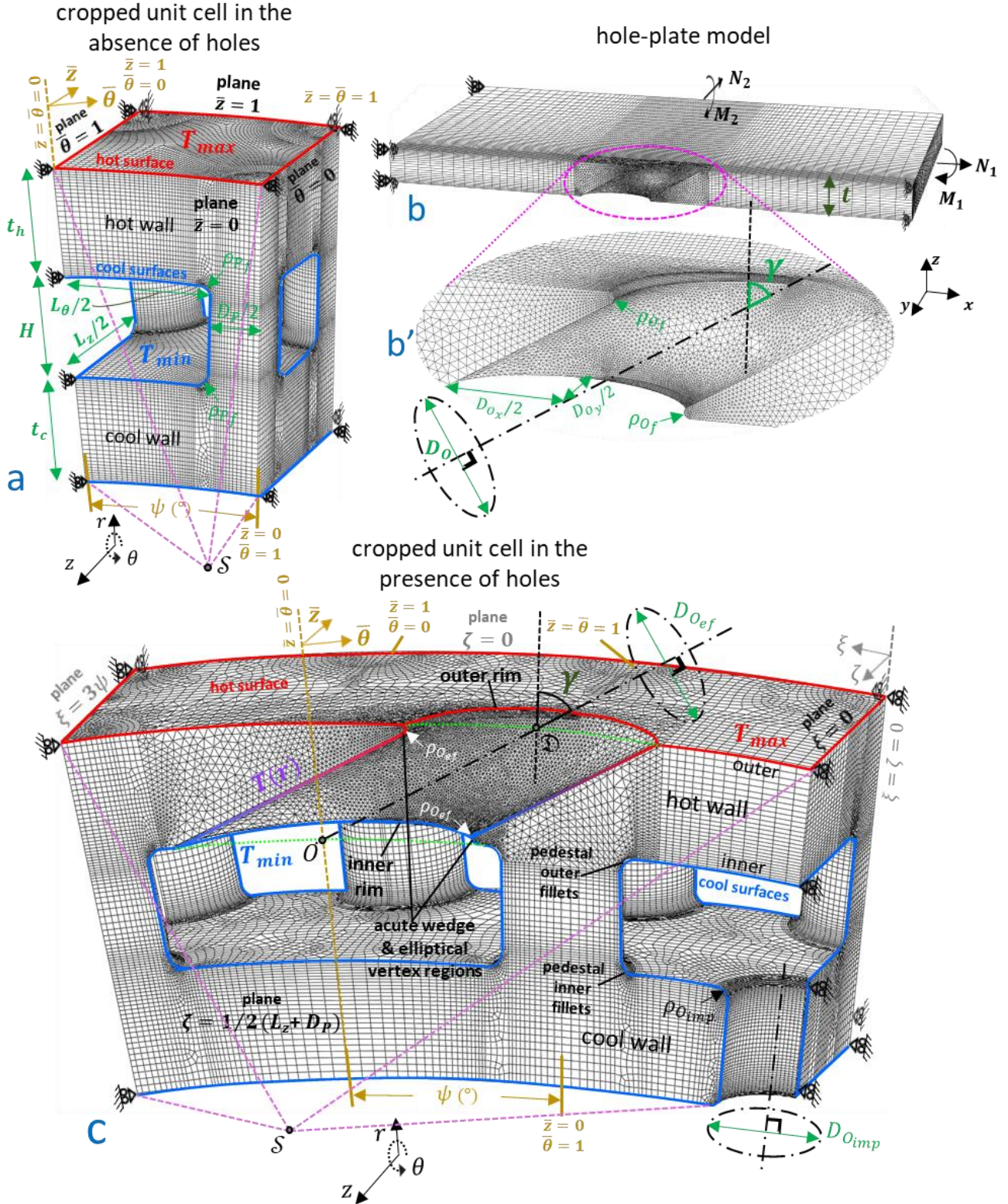


Figure 2. Illustration of FE models used to analyse the mechanical behaviour of the repeating unit cell in Figs 1b-b'. Images show: (a) cropped unit cell model used to study the nominal stresses in the absence of holes, (b) hole-flat plate model for oblique hole used to study stress concentrations, (b') detail of oblique hole (inclination and ellipticity are both present), and (c) cropped unit cell used to obtain full solutions in the presence of holes. Global-local coordinate systems, characteristic location, geometric dimensions and boundary conditions are denoted in the figures. Loading in Figs 1a, 1c is induced by prescribed maximum and minimum temperatures, T_{max} , T_{min} , whereas in Figs 1b-b' loading is applied through external membrane forces and bending moments.

The constraint cases A-B are also employed in Fig 2c. For case A, we apply common u_z between all the nodes at the $\zeta = 1/2(L_z + D_p)$ plane (see Fig 2c) and the reference node, \mathcal{S} , whereas for case B the plane $\zeta = 1/2(L_z + D_p)$ is set to deform into a conical surface of the form, $r = c_1 z + c_2$ (c_1 and c_2 are constants – see [28]). For the other three boundary planes, we use the same symmetry conditions for both cases A-B, including $u_\theta = 0$ for $\xi = 0$ and $\xi = 3\psi$, and $u_z = 0$ for $\zeta = 0$. The symmetry conditions at $\xi = 0$ and $\xi = 3\psi$, along with the use of 1/3rd of the actual unit cell (Fig 1b) in the FE domain (Fig 2c), are based on the assumption that the distances between adjacent effusion holes (see Fig 1b') are much larger than the respective hole sizes. In Fig 2c, this could practically require that the outer rim of the effusion hole is at sufficient distance from the boundaries of the domain, especially the $\xi = 0$ plane. This may not be true for extreme inclinations beyond the value of $\gamma = 60^\circ$ used in Fig 2c, combined with a narrow pedestal spacing, L_θ , in the θ direction. In such cases, periodic boundary conditions (cyclic symmetry) shall be used at $\xi = 0$ and $\xi = 3\psi$ in Fig 2c, i.e. by postulating the same u_θ displacement field at $\xi = 0$ and $\xi = 3\psi$. Similarly, an extremely small pedestal spacing, L_z , in the z direction in Fig 2c, would imply a very small distance between the effusion hole and the $\zeta = 0$ plane, and therefore one should include the entire unit cell of Fig 1b in the FE domain. The above extreme scenarios are not considered here, since Figs 1b-b' and Fig 2c correspond to the combination of parameters that gives the highest degree of asymmetry amongst all other configurations studied here, i.e. largest effusion hole diameter ratio, $\hat{D}_{of} = 1$, combined with largest inclination, $\gamma = 60^\circ$, and smallest possible pedestal spacing ratio, $\hat{L}_\theta = 1$. For this configuration, we performed preliminary simulations by using half (front side) of the unit cell in Fig 1b, repeated three times in the θ direction and by using the boundary conditions of case A. The results differed by only 1% in terms of the effusion hole peak stresses of the central unit cell, compared to the stresses obtained from the cropped model of Fig 2c. This confirmed that reducing the actual unit cell size (Fig 1b) and applying symmetry instead of periodic boundary conditions, does not compromise the current results.

3 Nominal stresses in the absence of holes

3.1 Nature of thermal stresses

FE results are firstly described in the absence of holes (Fig 2a) as shown in Figs 3-5. Figs 3a-b compare the kinematic structural response and FE contours of maximum absolute principal stress, $\sigma = \max(|\sigma_1|, |\sigma_2|, |\sigma_3|)$, normalised by $Ea\Delta T$, for constraint case A ($\varphi_{zh} = \varphi_{zc} = \varphi_{\theta h} = \varphi_{\theta c} = 0$) and case B ($\varphi_{zh} = \varphi_{zc} = 0$ & $\varphi_{\theta h} = \varphi_{\theta c} \neq 0$), for a large pedestal spacing, $\hat{L}_{\theta,z} = 5$, using a deformation scale factor of 50. Kinematically, the double wall system in case B extends in the z direction significantly more than in case A. Evidently, the requirement of equal wall z -extensions in case A implies that the cool wall imposes a more severe barrier to the thermal extension of the hot wall, compared to the requirement of equal wall θ -rotations of case B (where wall z -extensions are proportional). Hence, the smaller net thermoelastic z -extension of the system in case A, generates much larger membrane forces in the z direction compared to case B; these involve a compressive force (per unit length) through the hot wall and an equal and opposite tensile force in the cool wall i.e. $N_{zc} = -N_{zh}$. The effect of these larger membrane forces in case A is evident in Figs 3a-b by the higher compressive stresses in the hot surface and lower tensile stresses in the cool surface of the hot wall compared to case B. Another consequence is that the cool wall in case A experiences more severe tension than case B.

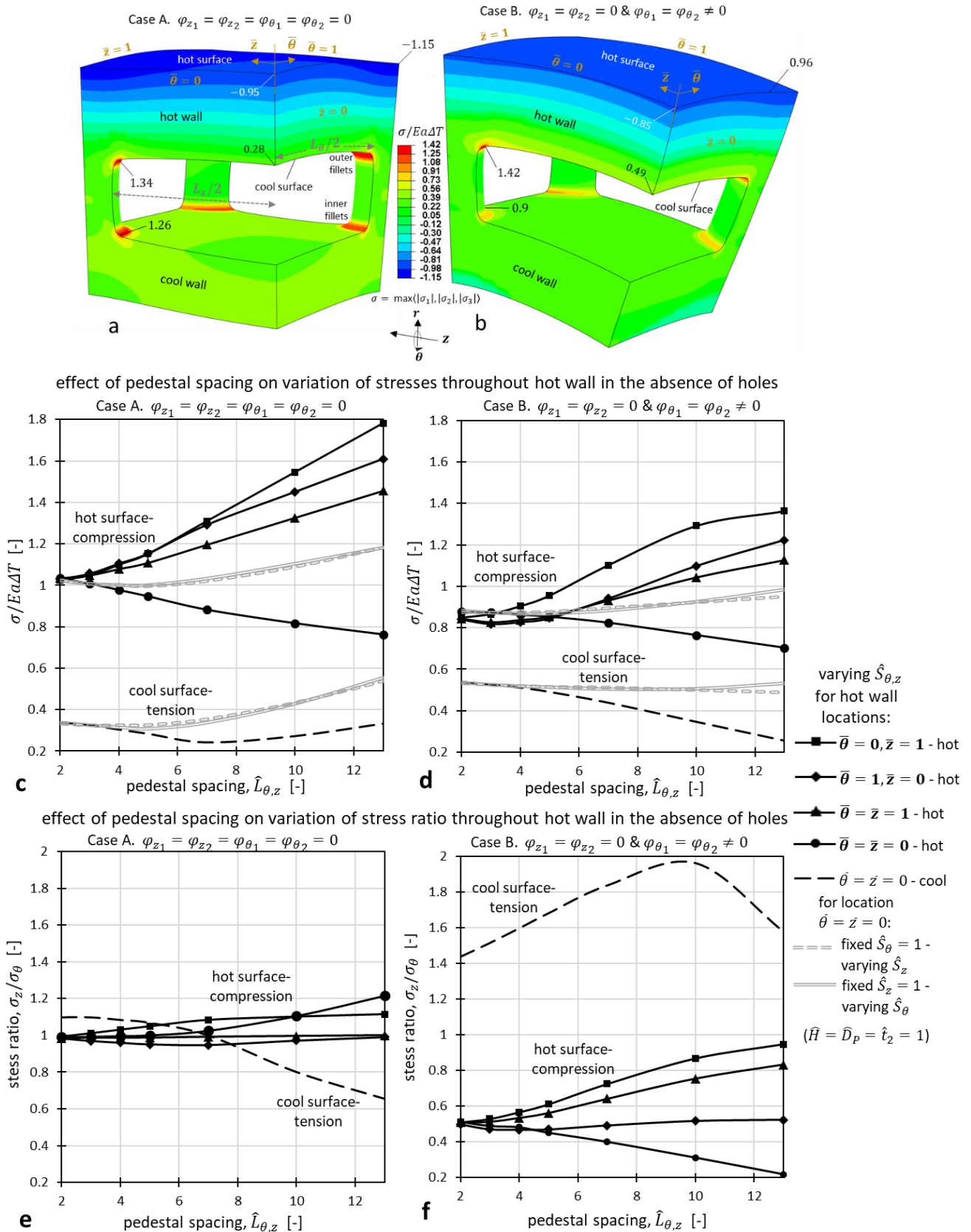


Figure 3. First set of results in the absence of holes (using FE model in Fig 2a). Fixed geometric ratios include: $\hat{R} = 20$, $\hat{t}_c = \hat{H} = \hat{D}_p = 1$, $\hat{p}_{Pf} = 0.1$. Images (a-b) compare maximum absolute principal stresses, σ , normalised with respect to $Ea\Delta T$, and the kinematic response for constraint case A (a) and case B (b) for the FE model in Fig 2a; with large pedestal spacing, $\hat{L}_{\theta,z} = 5$. Plots (c-d) show the variation of stresses at various surface locations in the hot wall, for cases A-B, versus pedestal spacing, $\hat{L}_{\theta,z}$. For the same hot wall locations, plots (e-f) display the variation of stress ratio, σ_z/σ_θ , for cases A-B.

Membrane forces along θ ($N_{\theta_c} = -N_{\theta_h}$) are induced in the same manner in both cases A-B, since the associated constraint $\varphi_{z_h} = \varphi_{z_c} = 0$ is the same. For the current thin wall systems i.e. $R/t_h = 20$, with small wall spacing, $R/H = 20$, the circumferential- θ wall extensions are approximately equal [28]. The latter is similar to the condition of common z -extensions of case A, which implies that thermal stresses in case A are induced in the same manner in the θ and z directions, constituting a nearly equibiaxial stress field. This is not true in case B which results in a general biaxial stress field in each wall. Triaxial stresses in both cases A-B exist only at the pedestal, and particularly at the pedestal-wall fillets, where acute tensile stress concentrations are developed (see Figs 3a-b). A major role of the pedestal is to prevent the two walls from moving apart, which has been shown [28] to induce a considerable tensile force i.e. tensile radial stresses (r direction), carried through the pedestal section. This force increases primarily with pedestal spacing, $\hat{L}_{\theta,z}$, and, secondarily, with cool wall thickness, \hat{t}_c ; for this reason, increasing \hat{t}_c and more importantly, $\hat{L}_{\theta,z}$, also requires large enough pedestal diameters, $\hat{D}_p = 1$, to avoid extreme tensile pedestal stresses.

3.2 Role of global geometric features

3.2.1 Pedestal spacing

Figs 3c-d shows that regardless of pedestal spacing, $\hat{L}_{\theta,z}$ ($\hat{L}_{\theta,z}$ denotes that \hat{L}_θ and \hat{L}_z vary equally) the compressive stresses at various locations of the hot surface are always much higher in case A than case B, while the opposite occurs for the tensile stresses at the cool surface of the hot wall. This relates to the much larger compressive membrane forces in the z direction through the hot wall in case A (as noted in Section 3.1). Figs 3c-d also show that in both cases A-B, compressive stresses at the hot surface above the pedestals, increase equally in θ , z directions, as $\hat{L}_{\theta,z}$ is increased, in contrast to the location, $\bar{\theta} = \bar{z} = 0$, away from the pedestals, where the stress decreases. From a theoretical perspective, this relates to the variation of bending moments and membrane forces with position, $\bar{\theta}, \bar{z}$, imposed by the presence of the tensile force carried through the pedestal. From a practical point of view, the nominal stress reduction at $\bar{\theta} = \bar{z} = 0$ is beneficial as this position corresponds to the effusion hole location.

From now on, we will consider $\bar{\theta} = \bar{z} = 0$ as the effusion hole location and focus on stresses at this particular point. Figs 3c-d provide additional results obtained by varying pedestal spacing differently in the θ and z directions, i.e. keeping \hat{L}_θ constant while varying \hat{L}_z and vice versa. In this case compressive and tensile stresses at $\bar{\theta} = \bar{z} = 0$ increase, although the effect comes into play at large \hat{L}_θ or \hat{L}_z . Of most significance here is the small pedestal spacing regime, i.e. $\hat{L}_{\theta,z} < 4$, since the aerothermal performance of the DWTC system is maximised at the minimum $\hat{L}_{\theta,z}$ [9]. For this regime, Figs 3e-f confirm Section 3.1 in that case A induces nearly equibiaxial stresses, i.e. stress ratios of $\sigma_z/\sigma_\theta \approx 1$ (Fig 3e), whereas constraint case B leads to biaxial stresses with $\sigma_z > \sigma_\theta$ in the tensile cool surface and $\sigma_z < \sigma_\theta$ in the hot compressive surface of the hot wall (see Fig 3f). The condition $\sigma_z > \sigma_\theta$ is attributed to the fact that in case B the bending moment about the θ axis in the hot wall dominates over the corresponding membrane force in the z direction, which is small in magnitude and tensile in nature; instead, $\sigma_z < \sigma_\theta$ is due to the fact that the membrane force in the θ direction makes a similar contribution to the corresponding moment about the z axis.

3.2.2 Wall thickness ratio – wall spacing

The stress ratio, σ_z/σ_θ , and the contribution of membrane forces are given particular emphasis here, as both will be shown to influence the SCF at the effusion hole. We parameterise the contribution of membrane force to a given stress by the term, $\% \bar{\sigma}/\sigma$, which is the percentage ratio of the average stress, $\bar{\sigma}$, through the wall thickness over the peak stress, σ , at the surface of interest. This implies that $-\infty < \% \bar{\sigma}/\sigma \leq \infty$ and that $\bar{\sigma}/\sigma = 100$, $\bar{\sigma}/\sigma = 0$ correspond to pure tension and pure bending, respectively; $\% \bar{\sigma}/\sigma < 0$ occurs when the surface stress is of opposite sign to the membrane force. In order to characterise the stress distribution at the effusion hole location, $\bar{\theta} = \bar{z} = 0$, in Figs 4a-d we fix $\hat{L}_{\theta,z} = 3$ and calculate $\% \bar{\sigma}/\sigma$ for the hot and cool surfaces of the hot wall, along θ and z for cases A-B, for different cool wall thickness, \hat{t}_c , and wall spacing, \hat{H} , values.

For the compressive surface stresses at the hot surface Fig 4a shows that in case A the compressive membrane forces contribute equally in both θ and z directions regardless of \hat{t}_c and \hat{H} , as opposed to case B (Fig 4c) where in the membrane force along z is tensile i.e. $\% \bar{\sigma}/\sigma < 0$. For tensile stresses at the cool surface, Fig 4b shows that in case A the membrane force contributions along θ and z are largely negative, while for case B (Fig 4d), the contribution along z is positive. Importantly, increasing \hat{t}_c in case A (Figs 4a-b) increases the compressive membrane forces (increasing the magnitude of $\% \bar{\sigma}/\sigma$), whereas the role of wall spacing, \hat{H} , is not at play. Indeed, the degree to which the cool wall impedes the thermal extension of the hot wall increases with \hat{t}_c , and does not depend on \hat{H} . The latter also implies that the bending moment in the hot wall is independent of geometry, in contrast to case B where bending moments apply in both walls and depend on both \hat{t}_c and \hat{H} (due to the condition of $\varphi_{\theta h} = \varphi_{\theta c} \neq 0$ – see Fig 3b).

In case B increasing \hat{t}_c in Figs 4c-d increases the compressive membrane force (increasing the magnitude of $\% \bar{\sigma}/\sigma$) along θ in a similar manner with case A. Increasing \hat{H} for $\hat{t}_c < 1.25$ reduces both the compressive force along θ (Fig 4c) and the tensile force along z (Fig 4d). As a result, the stress ratio, σ_z/σ_θ , in Figs 4e-f increases with \hat{H} both at the compressive and tensile surfaces of the hot wall, as opposed to case A where the stress states are constantly equibiaxial, i.e. $\sigma_z/\sigma_\theta \approx 1$.

3.2.3 Relationship between solutions in the absence and presence of a hole

The described effects of cool wall thickness, \hat{t}_c , and wall spacing, \hat{H} , on the stress ratio, σ_z/σ_θ , and membrane force contribution, $\% \bar{\sigma}/\sigma$, underpin the plots in Figs 5a-b, which compare the stresses at $\bar{\theta} = \bar{z} = 0$ in the absence of any holes (from Fig 2a) with those when effusion holes are present (from Fig 2c); in the latter case a fixed hole diameter, $\hat{D}_{o_{ef}} = 1$, and inclination, $\gamma = 60^\circ$, are used and the peak hole stresses mainly occur near the sharp regions of the outer and inner rim of the hole (denoted in Fig 2c). The peak compressive stress at the outer rim of the hole increases with \hat{t}_c in both cases A-B, as a result of the increase in the corresponding nominal compressive stress (see Figs 5a-b). The peak tensile stress at the inner hole rim decreases with \hat{t}_c in case A, owing to the reduction in the associated nominal stress (see Fig 5a). Instead, case B displays an increasing hole tensile stress with \hat{t}_c , in the regime, $\hat{t}_c < 1$, with the respective nominal tensile stress being less sensitive. The role of \hat{H} in both cases A-B is to mainly increase stresses both in the presence and absence of an effusion hole, with the effect being significant only for case B. The same discussion also explains the small sensitivity of the peak stresses at the pedestal fillets (computed from Fig 2a) with respect to \hat{H} for case A (see Fig 5c), as opposed to case B (see Fig 5d) where these stresses increase significantly with \hat{H} .

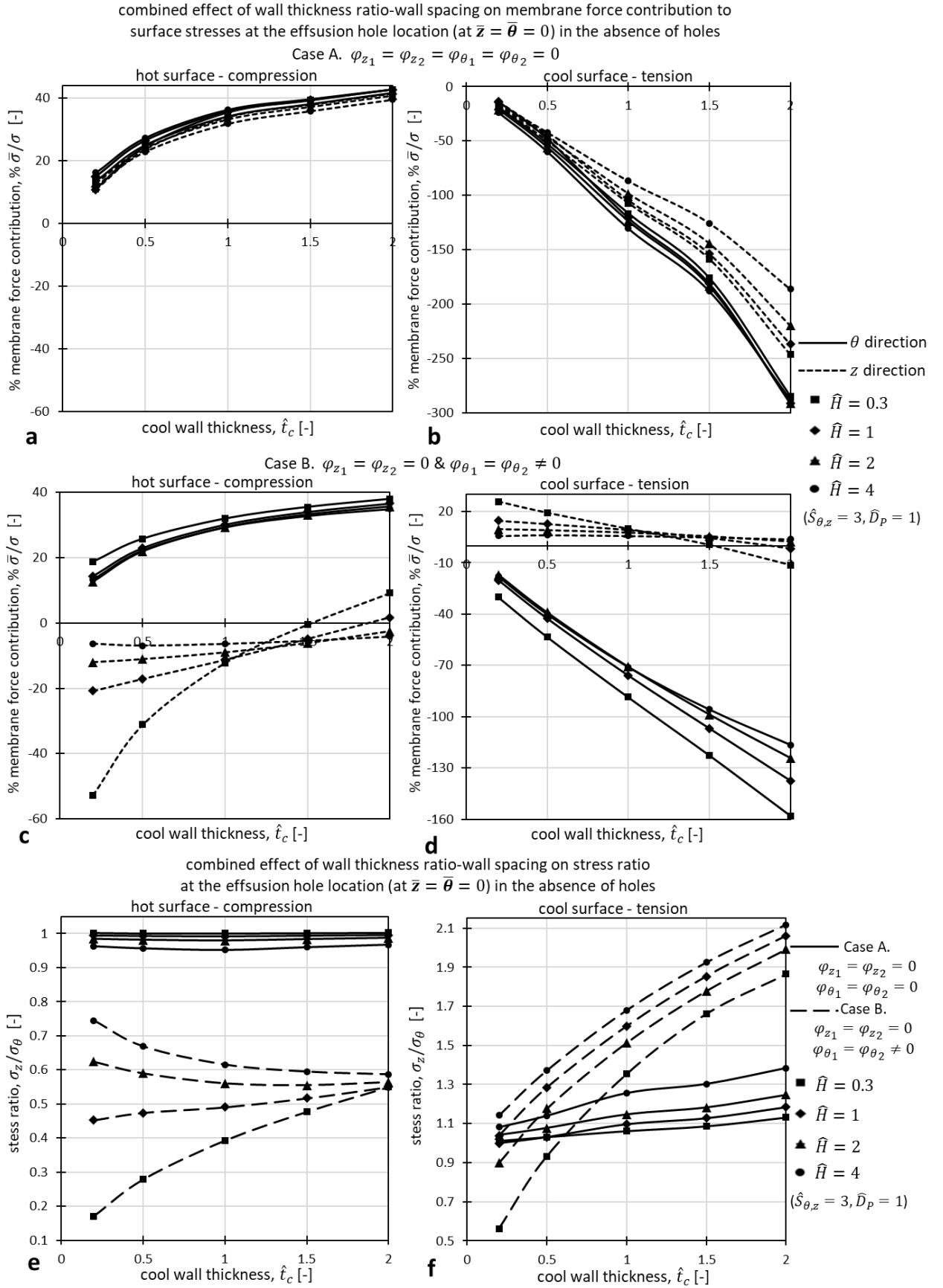


Figure 4. Second set of results in the absence of holes (using the FE model of Fig 2a). Fixed geometric ratios include: $\hat{R} = 20$, $\hat{L}_{\theta,z} = 3$, $\hat{D}_p = 1$, $\hat{p}_{pf} = 0.1$. Plots (a-b) for case A compare the percentage membrane force contribution parameter, $\% \bar{\sigma}/\sigma$, to stresses at the hot compressive surface (a) and cool tensile surface (b), at the effusion hole location, in the θ and z directions, for various cool wall thickness, \hat{t}_c , and wall spacing, \hat{H} , combinations. Plots (c-d) show the corresponding results for case B, while plots (e-f) show the variation of stress ratio, σ_z/σ_θ , with \hat{t}_c and \hat{H} , for cases A-B, for the same location.

Details of the pedestal fillet stresses are reported by the authors in [28]; here, we are interested in the magnitudes of these stresses compared to the effusion hole stresses. For case B, effusion hole tensile stresses (Fig 5b) are much larger than pedestal tensile stresses (Fig 5d) and effusion hole compressive stresses (Fig 5b), whereas in case A compression in the effusion hole is much more severe than tension (Fig 5a) as well as pedestal stresses (Fig 5d). Reducing \hat{t}_c decreases the compressive hole stress at the detriment of increasing the hole-pedestal tensile stresses, adding a trade-off within the design process. Effusion holes cause more critical stresses than pedestals; note however that this can change for large pedestal spacing and/or sharp pedestal fillets [28].

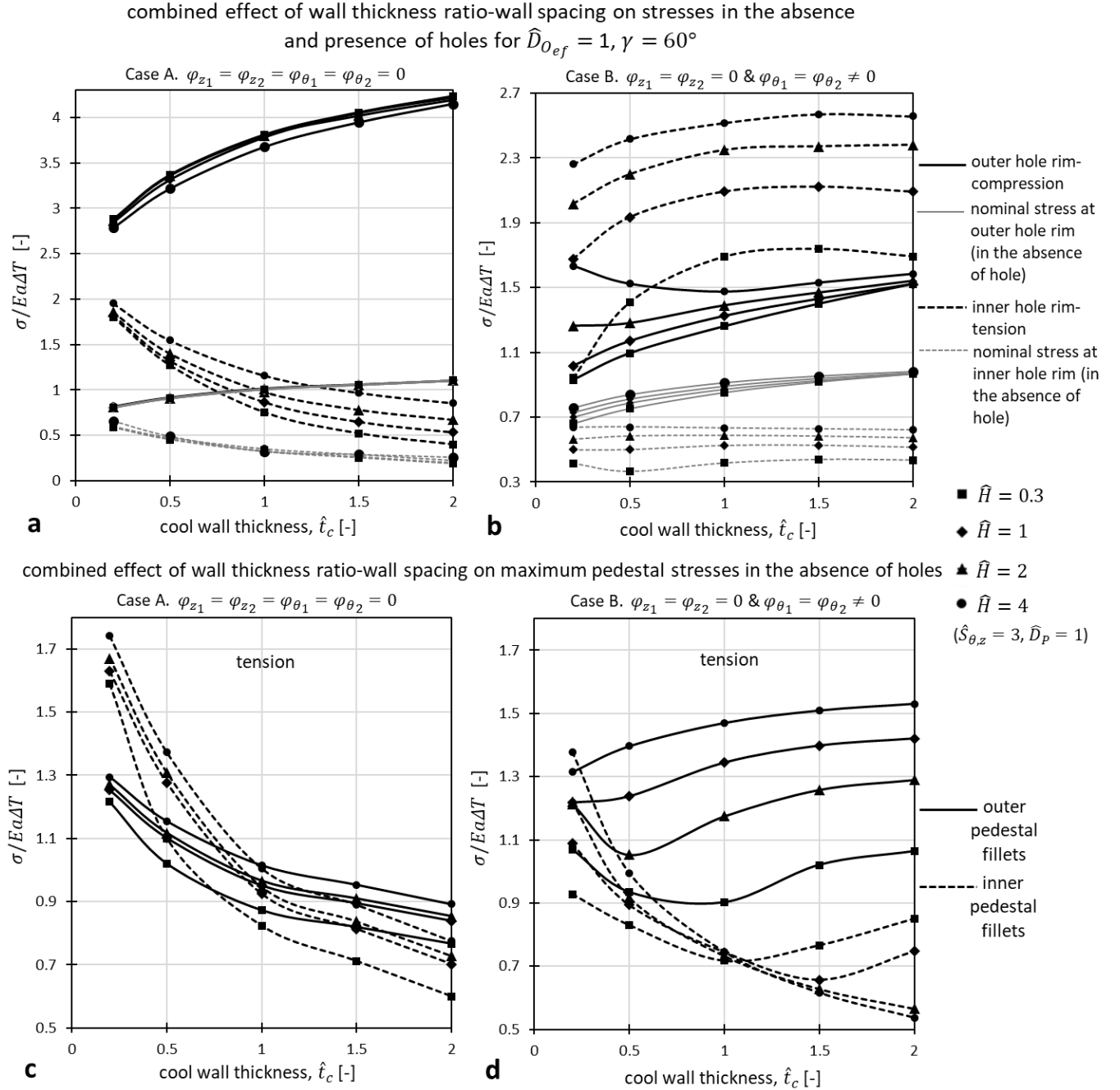


Figure 5. Final set of results in the absence of holes (using FE model in Fig 2a), together with results in the presence of holes (using FE model in Fig 2c). Fixed geometric ratios include: $\hat{R} = 20, \hat{L}_{\theta,z} = 3, \hat{D}_p = 1, \hat{p}_{pf} = 0.1$, and for the presence of holes: $\hat{D}_{O_{ef}} = \hat{D}_{O_{imp}} = 1, \gamma = 60^\circ, \hat{p}_{O_{ef}} = \hat{p}_{O_{imp}} = 0.05$. Plots (a-b) compare nominal compressive and tensile stresses at the location of the effusion hole in the absence of the hole compared to the corresponding peak stresses at the effusion hole when it is present, for cases A-B, and for varying cool wall thickness, \hat{t}_c , and wall spacing, \hat{H} combinations. Plots (c-d) show the effect of \hat{t}_c and \hat{H} on peak stresses at the outer and inner pedestal fillets.

4 Stresses in isolated holes

4.1 General analysis framework

To understand the origin of high stresses in effusion holes we firstly consider the fundamental problem of an isolated hole in a flat plate, subjected to membrane forces and moments in the two principal directions, x and y , as shown in Fig 2b. In many currently implemented film cooling technologies [19, 20, 43] the effusion holes are circular with a diameter, D , and are inclined at an angle, γ , to the wall surface normal. The intersections of the hole with the outer and inner surfaces of the wall produce elliptical rims, whose ellipticity is characterised by an aspect ratio, expressed in terms of the principal hole diameters in the plane of the wall as $D_{O_x}/D_{O_y} = 1/\cos\gamma$. The rims of the hole also have wedge-shaped profiles with a local wedge angle, ω , that varies along the circumference of the rims between an acute angle, $\omega = 90^\circ - \gamma$, and an obtuse angle, $\omega = 90^\circ + \gamma$. The orientation of the ellipse with respect to the in-plane principal stress directions provides an additional design variable. The maximum SCF at the effusion hole is known to increase with γ [34]. Here we will investigate whether this increase is dominated by the increase in ellipticity or increase in wedge angle. We will examine two different types of hole: a transverse elliptical hole ($D_{O_x}/D_{O_y} > 1$ and $\gamma = 0$, i.e. no inclination) and an inclined hole, whose ellipticity perpendicular to the axis of the hole is chosen to give a circular rim ($D_{O_x}/D_{O_y} = 1$ and $\gamma > 0$). The base feature for both of these holes is the transverse circular hole ($\gamma = 0$, $D_{O_x}/D_{O_y} = 1$) and this is analysed here first.

4.2 Transverse circular hole

We define the max SCF as the peak stress at the hole normalised by the peak stress in the plate when the hole is absent; maximum absolute principal stresses, $\sigma = \max(|\sigma_1|, |\sigma_2|, |\sigma_3|)$, are considered. For transverse holes ($\gamma = 0$) we find that under pure bending the max SCF occurs identically at the upper and lower rims of the hole, whereas with increasing membrane tension the location of the max SCF moves towards the mid-plane of the plate; the latter owes to 3D effects arising from the transition from plane stress towards plane strain conditions [29, 30].

For a fixed circular hole diameter over plate thickness ratio, $D_{O_y}/t = D_{O_x}/t = 0.7$, Fig 6a shows that the max SCF increases markedly as the through thickness nominal stress distribution switches from pure bending to pure tension, i.e. increasing $\% \bar{\sigma}/\sigma$. The effect is enhanced with decreasing σ_2/σ_1 (here σ_2/σ_1 denotes intermediate principal over maximum principal stress) and diminishes at the equibiaxial state, $\sigma_2/\sigma_1 = 1$ (Fig 6a) [34]. Bending is expected to reduce the SCF near holes-notches as it imposes a stress gradient across the plate, which is in opposition to the stress raising effect at the critical edge/surface feature. As a result, for the case $\% \bar{\sigma}/\sigma = -100\%$, where the rim of the hole is near the neutral axis, the max SCF reduces dramatically compared to the other $\% \bar{\sigma}/\sigma$ conditions in (Fig 6a). This phenomenon is relevant to the conditions at the inner rim of the effusion hole in our DWTC system for constraint case A, for which Fig 4b earlier showed that mainly negative $\% \bar{\sigma}/\sigma$ values occur in the cool surface of the hot wall. However, in case A equibiaxial stress states occur (shown earlier in Figs 4e-f) for which Fig 6a shows here that the SCF is not influenced by the through thickness stress distribution i.e. for $\sigma_2/\sigma_1 = 1$ the SCF is always equal to 2.

In agreement with previous studies [29, 30, 34], our FE 3D results in Fig 6a for pure tension display the expected $\sim 3\%$ increase with respect to the theoretical 2D (in-plane) solution, $\text{SCF} = 3 - \sigma_2/\sigma_1$. This increase is triggered by the Poisson's ratio, ν , effect, which induces a non-zero out-of-plane constraint factor, $F_z = \sigma_z/(\sigma_x + \sigma_y)$, with the implication that the SCF distribution depends

on the hole size ratio, D_{O_y}/t [29, 30]; note that $\sigma_x(= \sigma_1)$ and $\sigma_y(= \sigma_2)$ denote the in-plane stresses and σ_z denotes the out-of-plane stress and that $0 \leq F_z \leq \nu$ with $F_z = 0$ and $F_z = \nu$ for plane stress and plane strain 2D idealizations, respectively. The above 3D effect explains the fact that the max SCF occurs away from the hole rim with increasing tension in the plate and further indicates that this will depend on the ratio of the hole diameter to plate thickness, D_{O_y}/t [29, 30].

For the small hole, $D_{O_y}/t = 0.3$, a slightly lower max SCF in pure tension is observed in Fig 6b than for the larger holes, $D_{O_y}/t = 0.7, 1$ (this is consistent with [29, 30]), whereas the opposite occurs in pure bending (consistent with [34]). Combined tension-bending, i.e. $\% \bar{\sigma}/\sigma = 50\%$, leads to an intermediate response between pure tension and pure bending. We conclude that large transverse circular holes perform better in bending than small holes, with the effect vanishing for equibiaxial loading.

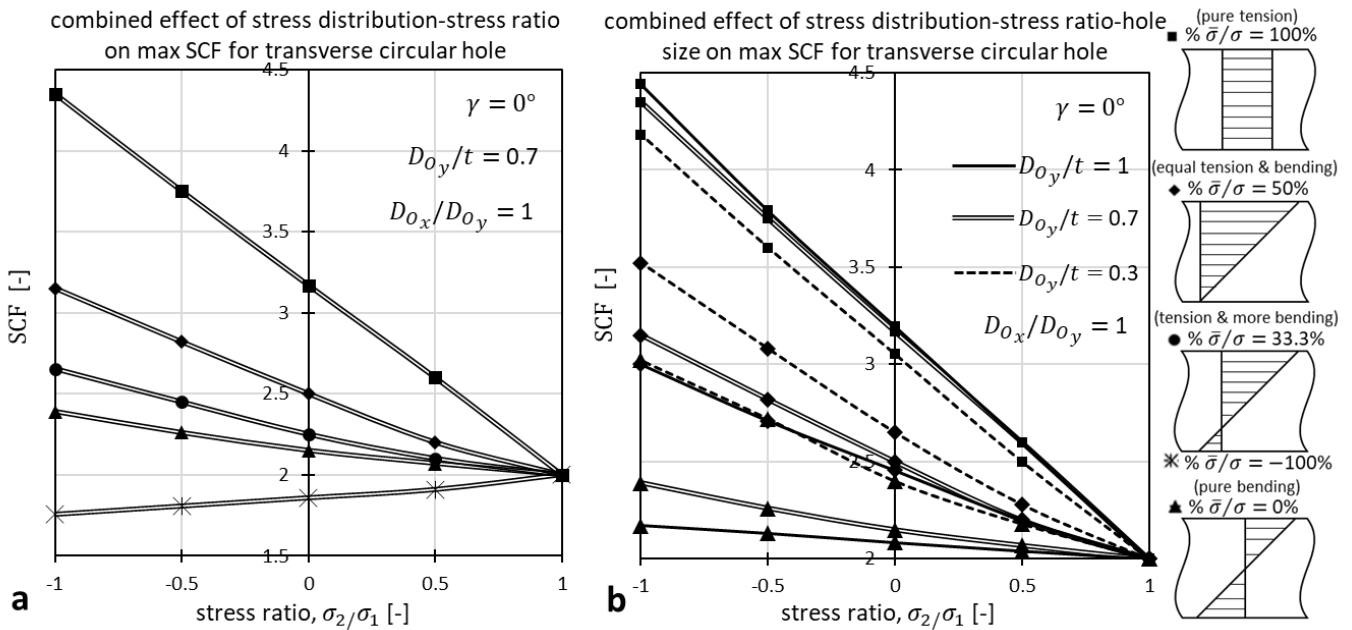


Figure 6. Stress concentration factors (SCF) for transverse circular holes in a large flat plate (using FE model in Fig 2b). For a single hole diameter to plate thickness ratio, $D_{O_y}/t = 0.7$, plot (a) shows the effect of stress ratio, σ_2/σ_1 , on maximum SCF, for different combinations of membrane force and moment, expressed in terms of the membrane parameter, $\% \bar{\sigma}/\sigma$. Plot (b) shows the effect of stress ratio, σ_2/σ_1 and hole size, D_{O_y}/t , on maximum SCF.

4.3 Transverse elliptical hole

We now examine the response when the ellipticity is increased by a factor of 2, i.e. $D_{O_x}/D_{O_y} = 2$. The FE contours in Figs 7a-d are obtained by normalising the peak stress at the hole over the peak stress in the plate in the absence of the hole (the same will be performed in Figs 8, 9). Figs 7a-d and 7e-h show that $D_{O_y}/t = 0.3$ generally gives larger max SCF than $D_{O_y}/t = 1$ in pure bending (consistent with [34]), while the opposite occurs in tension (consistent with [31]). In comparison to the SCF values shown earlier for the circular hole (Fig 6b), the addition feature here is that the SCF increases by a maximum amount at the elliptical vertex (Figs 7e,g) i.e. point of maximum curvature in the hole rim, and decreases by a maximum amount at the co-vertex (Figs 7f,h) i.e. point of

minimum curvature. This is a 2D (in-plane) effect and implies that for given biaxial state, σ_x/σ_y , and hole orientation, the max SCF can occur at any point along the hole rim. Equivalently, for given σ_x/σ_y the max SCF is minimised by rotating the hole about the z axis such that the max SCF occurs at the elliptical co-vertex. Figs 7e,g here are chosen to represent the worst case scenario, i.e. max SCF at the vertex when $-1 \leq \sigma_x/\sigma_y \leq 1$, whereas Figs 7f,h correspond to the best scenario, i.e. max SCF at the co-vertex when $-1 \leq \sigma_y/\sigma_x \leq 1$.

A consequence of the above 2D ellipticity effect in 3D space, is that for $\sigma_x/\sigma_y = 1$ (or $\sigma_y/\sigma_x = 1$) state, the max SCF is no longer independent of hole size and stress distribution through the thickness i.e. tension versus bending (see Figs 7e-h). This occurs only when the SCF is constant along the hole rim, implying that the theoretical 2D Inglis's solution [63], $\text{SCF} = (1 + 2D_{O_x}/D_{O_y}) - \sigma_x/\sigma_y$, for the vertex, must be equal to the solution, $\text{SCF} = (1 + 2D_{O_y}/D_{O_x}) - \sigma_y/\sigma_x$, for the co-vertex. Evidently, in Fig 7f the combination, $\sigma_y/\sigma_x = 0.5$ and $D_{O_x}/D_{O_y} = 2$, satisfies the above condition. Our FE 3D results in Figs 7e-h for pure tension are $\sim 6\%$ higher than the above theoretical 2D (in-plane) solutions, in agreement with [31-33]. We conclude that the significant increase of max SCF at the vertex of 3D elliptical holes is underpinned by 2D phenomena and that similar to transverse circular holes, decreasing hole size degrades the bending performance (see Figs 7e,g).

4.4 Inclined hole with circular rim

We now introduce inclination in a manner such that the hole rim remains circular in the $x - y$ plane i.e. $D_{O_x}/D_{O_y} = 1$. In this way we study the independent 3D effect of inclination, in the absence of ellipticity. As mentioned in Section 4.1, inclination, γ , produces wedge shaped hole rims of which the angle varies between $\omega = 90^\circ - \gamma$ (see Fig 8c) and $\omega = 90^\circ + \gamma$ (see Fig 8c); the intermediate wedge region where $\omega = 90^\circ$ (see Fig 8c) is here named '90° wedge region'. Figs 8a-h show that the max SCF increases with γ compared to the transverse circular hole. A new feature in Figs 8a-b, Fig 8d is that for $\sigma_x/\sigma_y = 1$, the max SCF can also occur near the 90° wedge depending on D_{O_y}/t . Indeed, for two inclinations, $\gamma = 30^\circ, 60^\circ$, Figs 8e-h indicate that when $\sigma_x/\sigma_y = 1$, the max SCF occurs in this region. In contrast, in Figs 8e-f the acute wedge region becomes more critical when $\sigma_x/\sigma_y < 0.5$ (Fig 8e), while the 90° wedge region experiences the max SCF when $\sigma_y/\sigma_x < 0.5$ (Fig 8f).

A theoretical basis for the above transition is non-existent. A relevant observation in Figs 8a-b is that the max SCF in the vicinity of the 90° wedge, consistently occurs at the hole rim, although for pure tension we would expect the max SCF to occur between the hole rim and the mid-plane. In contrast, the location of the peak SCF for the acute wedge regions in Figs 8a-b (SCF = 2.35 and SCF = 2.13) is translated towards the mid-plane, indicating that the out-of-plane constraint is different for different wedge angles. From a practical point of view, the main trend that small holes perform better in tension and worse in bending than large holes (shown earlier in Fig 6b, Figs 7e-h for transverse circular-elliptical holes), continues to apply for inclined holes, as shown in Figs 8e-h.

4.5 Inclined hole with elliptical rim

We now combine inclination with ellipticity such that the vicinity of the wedge angle, $\omega = 90^\circ - \gamma$, coincides with the vertex of the elliptical hole rim, while the 90° wedge region coincides with the

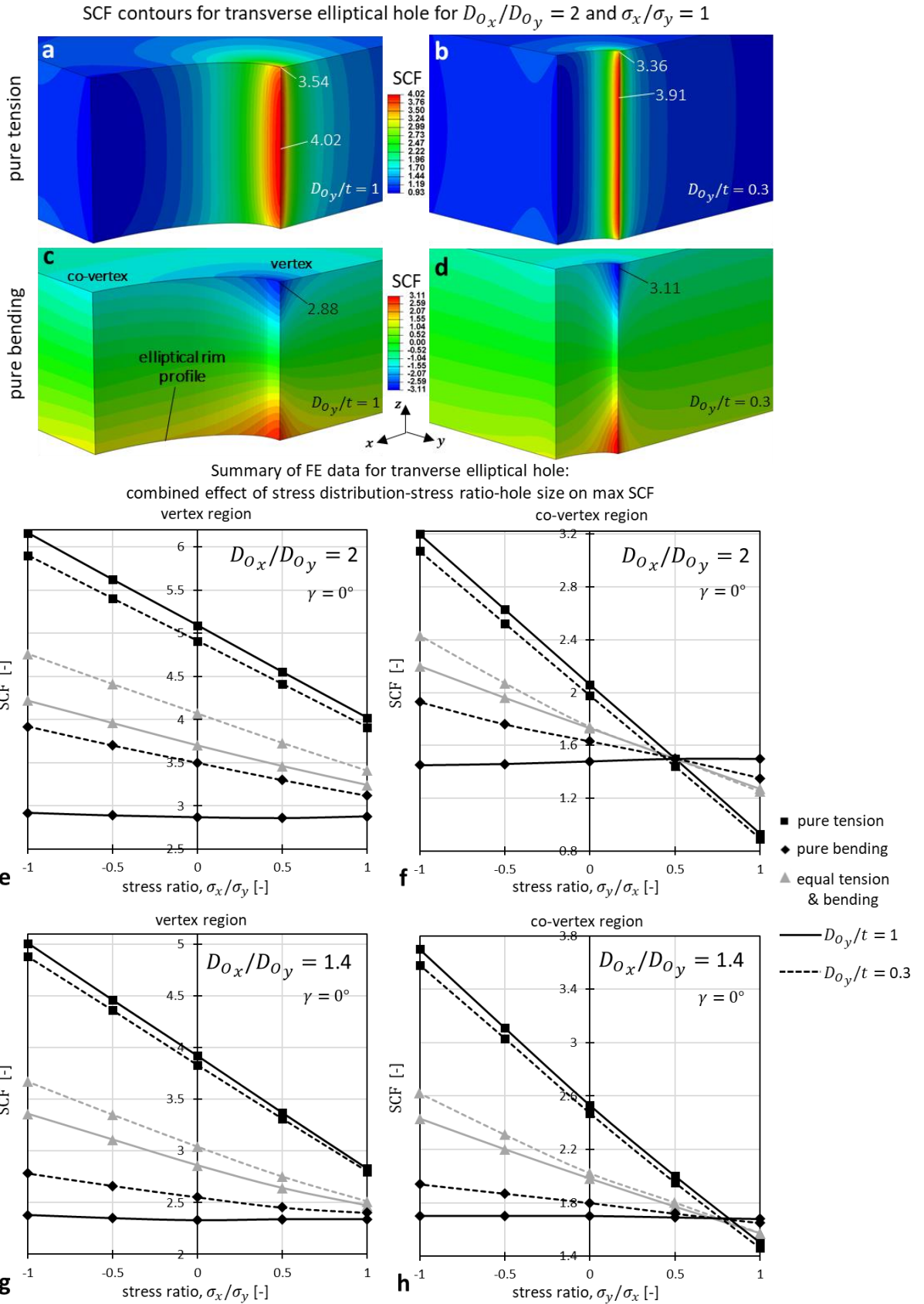
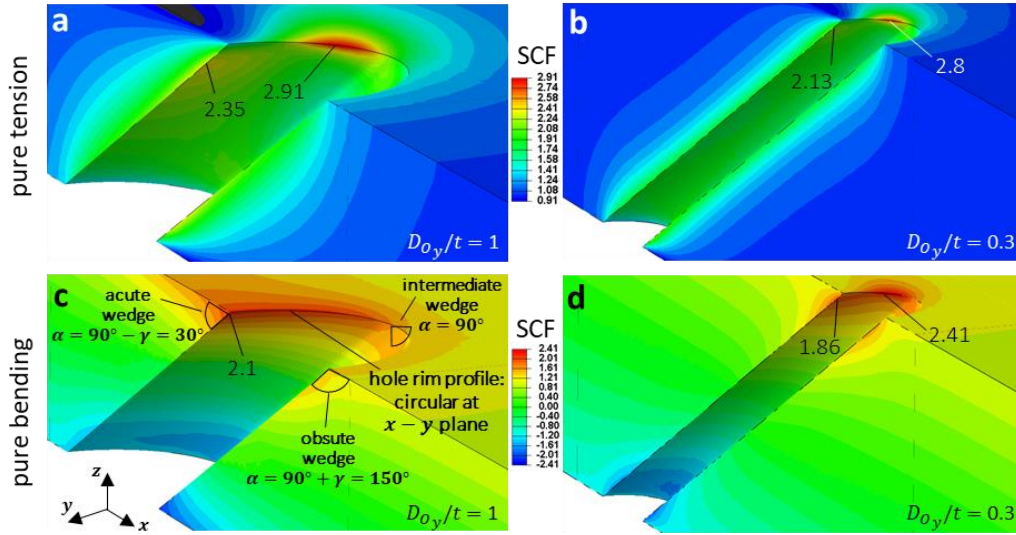


Figure 7. Stress concentration factors (SCF) for transverse elliptical holes in a large flat plate (using FE model in Fig 2b). For ellipticity, $D_{0x}/D_{0y} = 2$, and equibiaxial state, $\sigma_x/\sigma_y = 1$, (a-b) compare FE contours of maximum principal stress normalised with respect to the nominal stress at the hole, for a large hole size ratio, $D_{0y}/t = 1$, and a small ratio, $D_{0y}/t = 0.3$, in pure tension. The corresponding contours in pure bending are plotted in (c-d). Plots (e-h) show the maximum SCF at the hole for pure tension, pure bending and equal tension & bending for the large and small holes; for these conditions, plots (e) and (g) show the effect of stress ratio, σ_x/σ_y , on the maximum SCF in the vicinity of the elliptical vertex for ellipticities $D_{0x}/D_{0y} = 2$ and $D_{0x}/D_{0y} = 1.4$, respectively. For the same ellipticities, plots (f) and (h) show the effect of σ_y/σ_x on the maximum SCF in the vicinity of the elliptical co-vertex.

SCF contours for inclined hole with circular rim ($D_{0x}/D_{0y} = 1$) for $\gamma = 60^\circ$ and $\sigma_x/\sigma_y = 1$



Summary of FE data for inclined hole with circular rim:

combined effect of stress distribution-stress ratio-hole size on max SCF

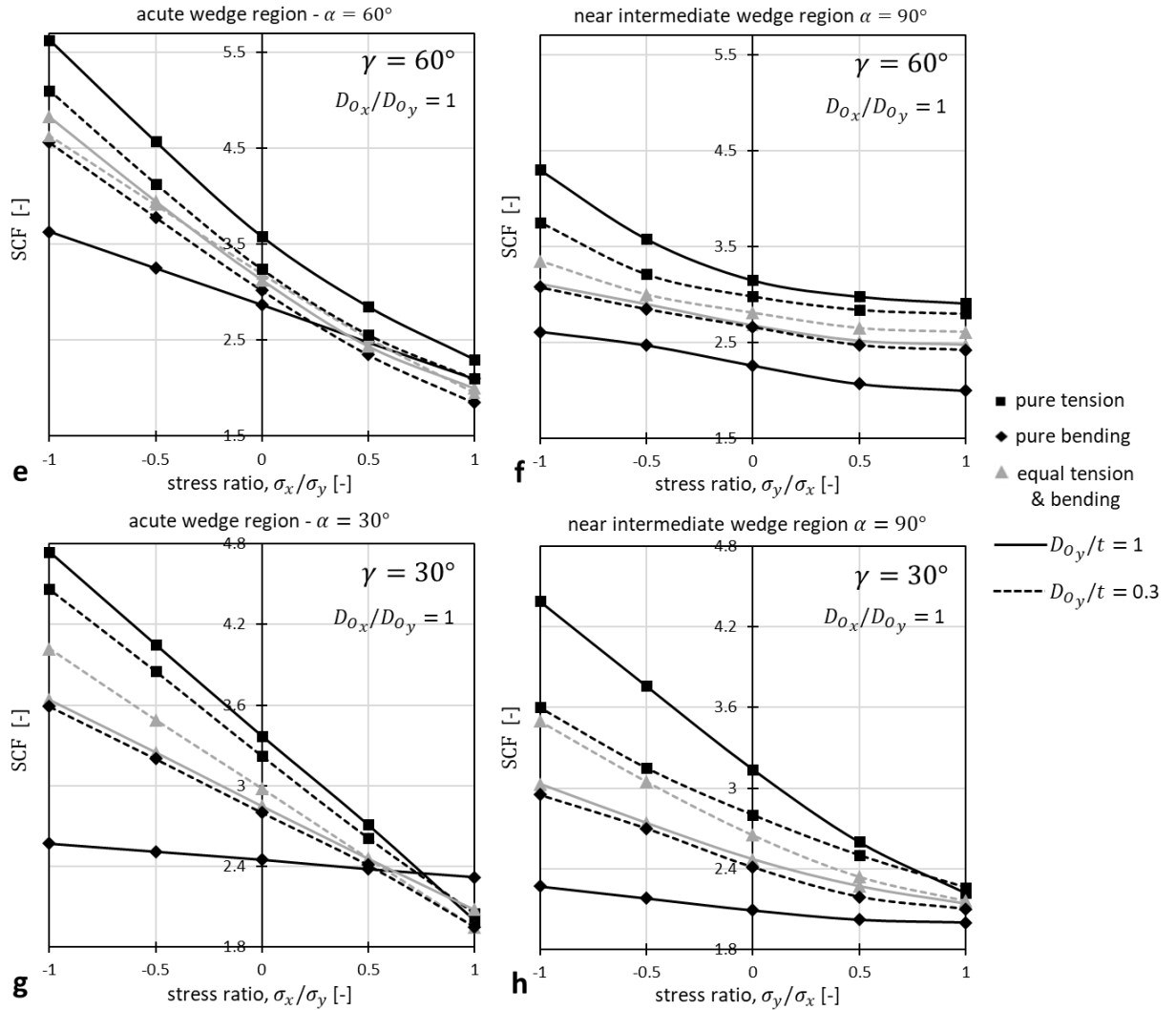


Figure 8. Stress concentration factors (SCF) for inclined holes with circular rim in a large flat plate (using FE model in Fig 2b). For inclination, $\gamma = 60^\circ$, and equibiaxial state, $\sigma_x/\sigma_y = 1$, (a-b) compare FE contours of the maximum principal stress normalised by the nominal stress for a large hole size ratio, $D_{0y}/t = 1$, and a small ratio, $D_{0y}/t = 0.3$, in pure tension. The respective contours in pure bending are plotted in (c-d). Plots (e-h) display the maximum SCF for pure tension, pure bending and equal tension & bending for the large and small holes; for the following cases: (e) and (g) show the effect of stress ratio, σ_x/σ_y , on the maximum SCF in the acute wedge region of the hole rim, for inclinations, $\gamma = 60^\circ$, and $\gamma = 45^\circ$, respectively; while for the same inclinations, (f) and (h) show the effect of σ_y/σ_x on the maximum SCF near the intermediate 90° wedge.

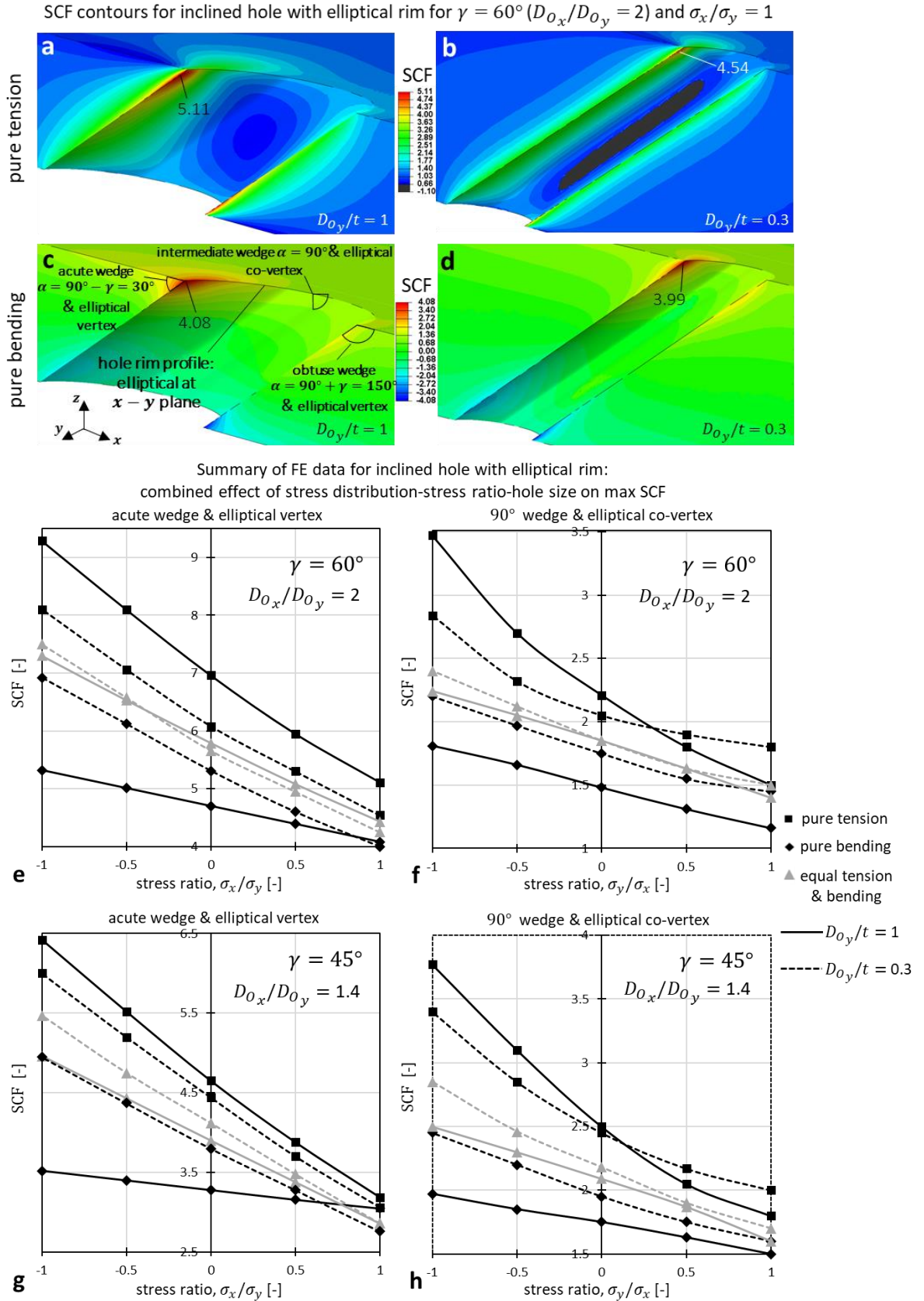


Figure 9. Stress concentration factors (SCF) for inclined holes with elliptical rim in a large flat plate (using FE model in Fig 2b). For inclination, $\gamma = 60^\circ$, ellipticity, $D_{0x}/D_{0y} = 2$, and equibiaxial state, $\sigma_x/\sigma_y = 1$, (a-b) compare FE contours of maximum principal stress normalised by the nominal stress for a large hole size ratio, $D_{0y}/t = 1$, and a small ratio, $D_{0y}/t = 0.3$, in pure tension. The respective contours in pure bending are plotted in (c-d). Plots (e-h) provide the maximum SCF for pure tension, pure bending and equal tension & bending for the large and small holes; for these situations: (e) and (g) show the effect of stress ratio, σ_x/σ_y , on the maximum SCF near the acute wedge-elliptical vertex of the hole rim, for the combination, $\gamma = 60^\circ$, $D_{0x}/D_{0y} = 2$, and, $\gamma = 45^\circ$, $D_{0x}/D_{0y} = 1.4$, respectively. For the same combinations, (f) and (h) show the effect of σ_y/σ_x on the maximum SCF in the intermediate 90° wedge-elliptical co-vertex region.

independent & combined effect of ellipticity and inclination on max SCF for different hole size, stress distribution and between tension & bending

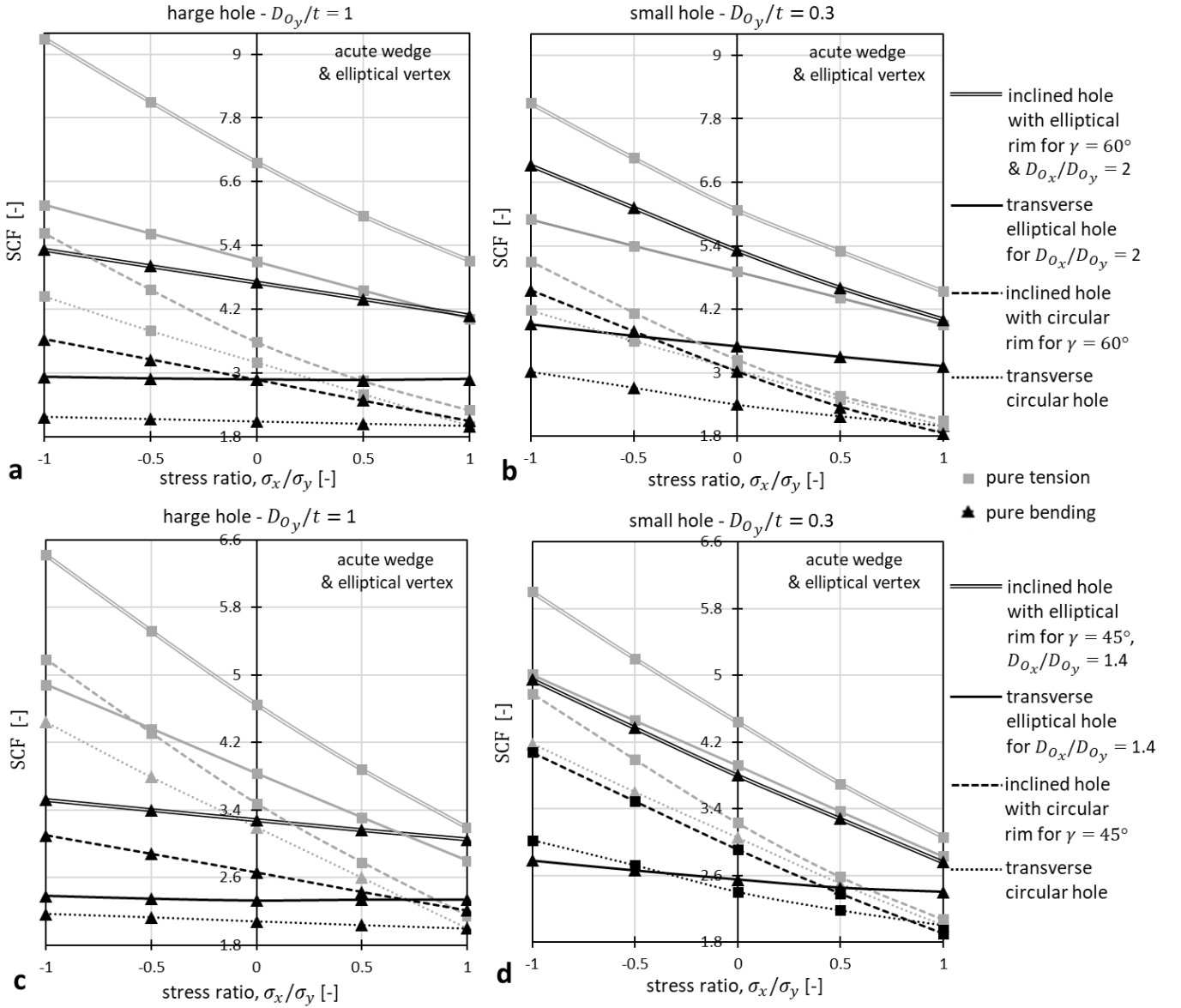


Figure 10. Comparison of stress concentration factors (SCF) for four hole geometries (using FE model in Fig 2b). All plots (a-d) show the maximum SCF in the acute wedge region of the hole rim, as a function of stress ratio, σ_x/σ_y , in pure tension and pure bending. Plots (a-b) compare results for a large hole size ratio, $D_{o_y}/t = 1$, and a small hole, $D_{o_y}/t = 0.3$, for transverse circular holes, inclined holes at $\gamma = 60^\circ$ with circular rim, transverse holes with ellipticity, $D_{o_x}/D_{o_y} = 2$, and inclined holes at $\gamma = 60^\circ$ with elliptical rim of $D_{o_x}/D_{o_y} = 2$. Plots (c-d) show the corresponding results when inclinations of $\gamma = 45^\circ$ and ellipticities of $D_{o_x}/D_{o_y} = 1.4$ are used.

co-vertex. Our data in Fig 9g for pure tension and $\gamma = 45^\circ$ agree with previous work [34] for the acute wedge-elliptical vertex region, while the literature on oblique holes under bending is sparse. In Figs 9e-h we focus on the nominal stress conditions that apply in the effusion hole location in the actual DWTC system (Figs 4a-d), for case A. These involve a membrane force contribution of $\% \bar{\sigma}/\sigma = 33.3$ at the compressive hot surface and a $\% \bar{\sigma}/\sigma = -100$ at the cool surface. The $\% \bar{\sigma}/\sigma = 33.3$ suggests that the SCF results between pure bending ($\% \bar{\sigma}/\sigma = 0$) and ‘equal tension & bending’ ($\% \bar{\sigma}/\sigma = 50$) are of interest in Figs 9e-h, whereas $\% \bar{\sigma}/\sigma = -100$ is relevant to the results of Figs 9e-h for pure bending; the latter is based on the strong influence of the bending stress distribution on the SCF for $\% \bar{\sigma}/\sigma < 0$, as discussed in Section 4.2. The σ_x/σ_y ratios of interest are

in the range, $0.5 < \sigma_x/\sigma_y \leq 1$, with $\sigma_x/\sigma_y = 1$ being the most important (Fig 4e-f). For the above range of conditions, we conclude that the small hole, $D_{o_y}/t = 0.3$, provides the lowest max SCF in both the acute wedge and 90° wedge regions of the hole rim, compared to the larger hole, $D_{o_y}/t = 1$ (Figs 9e-h). This trend is consistent with the results on transverse circular-elliptical holes and inclined holes with circular rim.

Acute wedge-elliptical vertex regions (Figs 9e,g) associate with a drastically higher SCF compared to the 90° wedge-elliptical co-vertex regions (Figs 9f,h), especially at large γ . The effect of γ is reported in the literature [34, 40, 41], and is expected to arise due to the synergy of inclination and ellipticity, which both enhance the SCF in the acute wedge-elliptical vertex region. However, the contributions of ellipticity and inclination have not been reported. This is addressed by Figs 10a-d, where we combine SCF results for the co-vertex of the transverse elliptical hole rim, for the acute wedge of the inclined hole with circular rim, and for the acute wedge-elliptical vertex region of the inclined hole with elliptical rim; results for the transverse circular hole are also provided. Ellipticity alone is shown to increase the max SCF by a markedly higher degree than inclination alone (Figs 10a-d), especially in pure tension.

We therefore conclude that the 2D effect of ellipticity plays a more significant role than the 3D effect of inclination on the total increase of SCF that occurs when these two effects are combined. It is also highlighted that inclined holes with circular rims instead of elliptical rims, reduce drastically the max SCF. This reduction is shown to be far more significant than the potential reductions achieved by modifying hole size, especially for the equibiaxial stress states of interest. The latter, however, is strictly based on calculations for holes in an infinite plate. The relevance of these calculations to the actual effusion hole response in the actual DWTC system is studied next.

5 Peak stresses in the presence of holes

5.1 Nature of the response in the presence of holes

The response of the DWTC system in the presence of holes is illustrated the FE contours in Figs 11a-h; these represent maximum absolute principal stress, $\sigma = \max\{|\sigma_1|, |\sigma_2|, |\sigma_3|\}$, normalised by $Ea\Delta T$. Figs 11a-b compare the kinematic response of the system for constraint case A ($\varphi_{z_h} = \varphi_{z_c} = \varphi_{\theta_h} = \varphi_{\theta_c} = 0$) and case B ($\varphi_{z_h} = \varphi_{z_c} = 0$ & $\varphi_{\theta_h} = \varphi_{\theta_c} \neq 0$), for a large pedestal spacing, $\hat{L}_{\theta,z} = 13$. We also show the deformed configuration using a deformation scale factor of 50. The major features of the response for each of these cases, are equivalent to those in the absence of holes, illustrated earlier in Figs 3a-b for $\hat{L}_{\theta,z} = 5$. These features include (Figs 11a-b) the larger compressive stresses at the hot outer surface in case A compared to case B, as well as the increase of these stresses near the pedestals in both cases. In addition, Figs 11a-b also highlight that for a very large pedestal spacing, $\hat{L}_{\theta,z} = 13$, pedestal stresses can be as critical as effusion hole stresses; this is due to the large tensile forces carried through the pedestals to constrain the hot wall from moving away from the cool wall, in the radial r direction.

The above scenario of $\hat{L}_{\theta,z} = 13$ represents an extreme case, for which previous heat transfer studies suggest a weak cooling performance [9]. The opposite extreme scenario, of greater interest is when $\hat{L}_{\theta,z}$ is minimised. This is represented in Figs 11c-d by $\hat{L}_{\theta,z} = 3$, which is as small as possible for an effusion hole of $\hat{D}_{o_{ef}} = 1$ and $\gamma = 60^\circ$. Note that the geometry of Figs 11c-d is identical to the FE model in Fig 2c and corresponds to the results of Figs 5a-d. Figs 11c-d highlight that effusion hole stresses are more critical than stresses at the pedestal fillets and impingement holes.

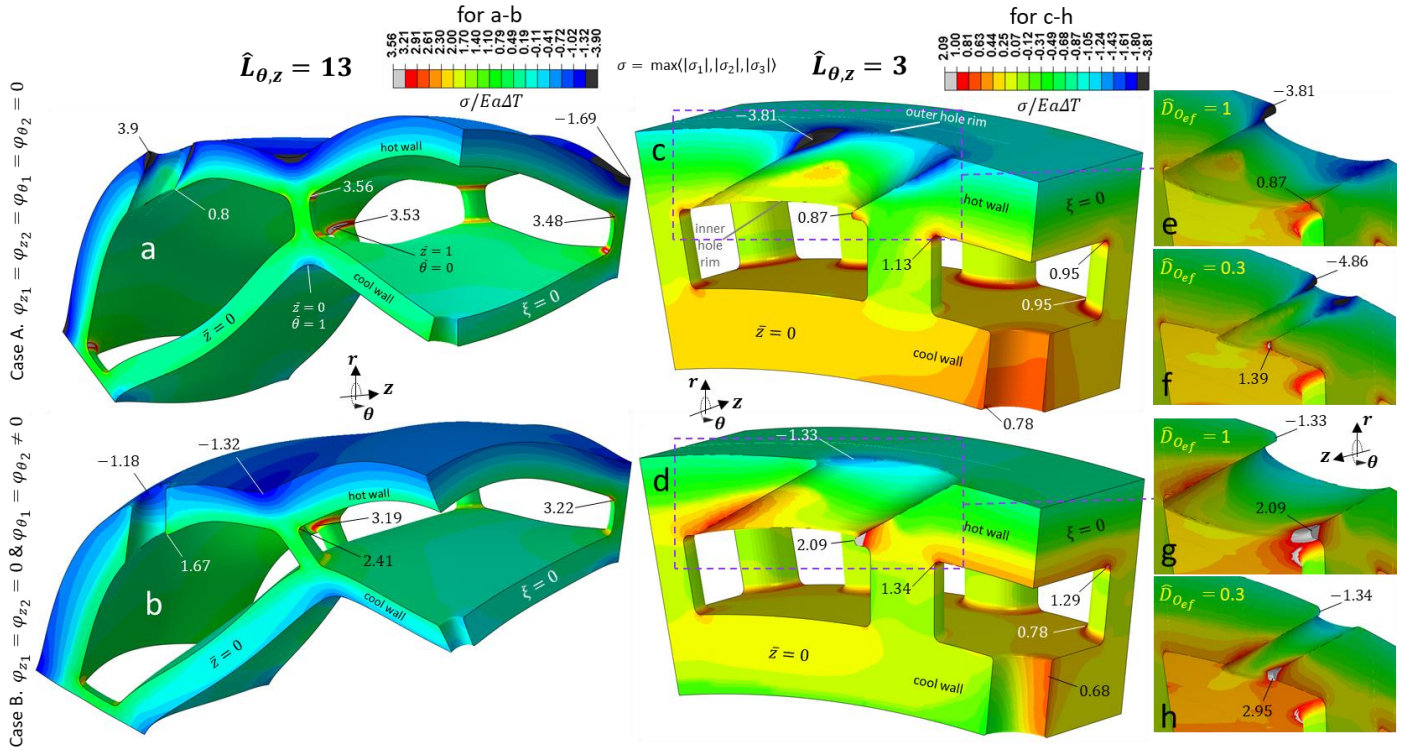


Figure 11. Representative FE contours of maximum absolute principal stresses, σ , normalised with respect to $Ea\Delta T$, in the presence of holes for the FE model of Fig 2c. Fixed geometric ratios include: $\hat{R} = 20$, $\hat{t}_c = \hat{H} = \hat{D}_p = 1$, $\hat{\rho}_{pf} = 0.1$, $\gamma = 60^\circ$, $\hat{\rho}_{0ef} = \hat{\rho}_{0imp} = 0.05$. (a-b) compare peak stresses and the kinematic response for constraint case A (a) and case B (b) for a large pedestal spacing, $\hat{L}_{\theta,z} = 13$, and effusion and impingement hole size, $\hat{D}_{0ef} = \hat{D}_{0imp} = 1$. For the same hole sizes, (c-d) compare peak stresses for cases A-B for the smallest possible pedestal spacing, $\hat{L}_{\theta,z} = 3$. (e) and (g) provide detailed effusion hole views of the contours in (c) and (d), respectively; these are compared with the corresponding contours (f) and (h), for the small effusion and impingement holes, $\hat{D}_{0ef} = \hat{D}_{0imp} = 0.3$.

As shown earlier in Figs 5a-b, case B (Fig 11d) leads to a higher peak tensile stress at the acute wedge-elliptical vertex of the inner rim of the effusion hole than case A (Fig 11c). On the basis of our solutions in the absence of holes and our independent oblique hole-plate analysis, the above effect is due to the following three conditions that occur at the inner rim of the effusion hole (in the absence of the hole) in case B compared to case A:

- (a) higher nominal tensile stresses (shown in Figs 5a-b for $\hat{t}_c = \hat{H} = 1$);
- (b) higher nominal stress ratio, σ_z/σ_θ (shown in Figs 4e-f for $\hat{t}_c = \hat{H} = 1$), which enhances the SCF in the acute wedge-elliptical vertex region;
- (c) positive membrane force contribution, $\% \bar{\sigma}/\sigma$, along z (shown in Figs 4b,d for $\hat{t}_c = \hat{H} = 1$) which enhances further the SCF with respect to the condition $\% \bar{\sigma}/\sigma < 0$ for case A in both θ and z directions.

Equivalent factors also explain the much higher peak compressive stress at the outer hot rim of the effusion hole in case A (Figs 11a,c), compared to case B (Fig 11b,d). Figs 11a,c highlight that the nearly equibiaxial nominal stress state, $\sigma_z/\sigma_\theta \approx 1$, in case A (shown earlier in Figs 4e) induces the max SCF in the acute wedge-elliptical vertex of the outer rim of the effusion hole; this maximises the peak compressive hole stress. In contrast, Figs 11b,d shows that for case B where $\sigma_z/\sigma_\theta \approx 0.5$ (shown in Figs 4e for $\hat{t}_c = \hat{H} = 1$), the location of the max SCF is transposed towards the 90° wedge-elliptical co-vertex of the effusion hole rim; this minimises the peak compressive hole stress.

The above characteristics between cases A-B for the hole size $\hat{D}_{0ef} = 1$ (Figs 11a-d), also apply for the smaller hole, $\hat{D}_{0ef} = 0.3$, as evidenced by comparing the responses for the two hole sizes in Figs 11e-f (case A) and Figs 11g-h (case B). The location of max SCF for each case does not change

with hole size, but the peak compressive and tensile stresses are drastically modified, with the small hole leading to much larger stresses. The latter conflicts with our earlier conclusions on the hole-plate analysis (Section 4.5), that $\hat{D}_{O_{ef}} = 0.3$ gives lower max SCF than $\hat{D}_{O_{ef}} = 1$. This indicates that the max SCF at the hole is affected by hole-hole and hole-pedestal interactions, as well as, potentially, by the decrease of the overall stiffness of the system at high porosities i.e. at high $\hat{D}_{O_{ef}}/\hat{L}_{\theta,z}$ ratios. Sensibly, the large hole enhances the interaction effects along with the overall effect of porosity, while increasing γ increases the porosity for a fixed $\hat{D}_{O_{ef}}$. We can also note that for the large hole (Figs 11e,g) the acute wedge-elliptical vertex of the inner hole rim is closer to the neighbouring pedestal fillet, compared to the small hole (Figs 11f,h); the opposite is the case for the acute wedge-elliptical vertex of the outer hole rim and the pedestal. All The above suggest that the interaction and porosity effects are influenced by the hole size, $\hat{D}_{O_{ef}}$, hole inclination, γ , and pedestal spacing, $\hat{L}_{\theta,z}$. In this study we do not decouple the interaction and porosity effects, but instead focus on how the stress state in the vicinity of the effusion hole varies within a wide range of values of $\hat{D}_{O_{ef}}$, γ and $\hat{L}_{\theta,z}$.

5.2 Interplay between pedestal spacing, hole size and hole inclination

5.2.1 The role of effusion hole inclination

The combined effect of $\hat{D}_{O_{ef}}$, γ and $\hat{L}_{\theta,z}$ on the effusion hole stresses is illustrated by Figs 12a-d. Figs 13a-h' also compares the max SCFs results between two different calculations:

- (a) a direct calculation of max SCF by normalising the peak hole stresses in Figs 12a-d with the nominal stresses at the corresponding hole locations (for each combination of $\hat{L}_{\theta,z}$, $\hat{D}_{O_{ef}}$, γ) obtained from the model in Figs 3a-b;
- (b) an indirect calculation of the max SCF by using the nominal stresses at the peak hole stress locations in Figs 3a-b, to determine appropriate bending moments and membrane forces in the θ and z directions, which are then employed in the hole-plate model of Fig 2b.

The inclination, γ , has a large effect on both the peak compressive and tensile stresses for case A (Figs 12a-b), in agreement with our independent hole-plate analysis and the corresponding increase of max SCF with increasing γ in Figs 13a-h (for both calculations). For case B, this trend is only observed for the peak tensile stresses (Fig 12d and Fig 13b',d',f',h'), as the compressive stresses (Fig 12c) and the corresponding SCFs (Figs 13a',c',e',g') both decrease with γ . This is because, in contrast to all the other peak stresses, the peak compressive stresses in case B consistently occur in the 90° wedge-elliptical co-vertex of the outer hole rim (shown earlier in Figs 11b,d), rather than in the acute wedge-elliptical vertex; in this case, increasing inclination, γ , decreases the hole ellipticity, D_{O_y}/D_{O_x} , such that the SCF at the 90° wedge-elliptical co-vertex region increases (Figs 13a',c',e',g'). A similar phenomenon explains the increase of peak tensile stresses in Fig 12b with $\hat{L}_{\theta,z}$ for $\hat{L}_{\theta,z} > 7$, when $\gamma = 30^\circ$ and especially for $\gamma = 0^\circ$. Here, the effect is induced by the gradual decrease of σ_z/σ_θ for $\hat{L}_{\theta,z} > 7$ shown earlier in Fig 3e, which transposes the location of max SCF from the 90° wedge to the acute wedge of the elliptical hole rim. Evidently, in Figs 13b,d the SCF clearly decreases for $\hat{L}_{\theta,z} > 7$ when $\gamma = 45^\circ$ and $\gamma = 60^\circ$ and increases in Fig 13h for $\gamma = 0^\circ$.

5.2.2 The role of pedestal spacing

Except for the above cases, inclination, γ , does not (Figs 12a-d) qualitatively change the way the peak stresses (Figs 12a-d) and associated SCFs (Figs 13a-h') vary with $\hat{L}_{\theta,z}$ and $\hat{D}_{O_{ef}}$, suggesting that the interaction effects mainly occur in a similar manner for inclined and transverse holes. For the

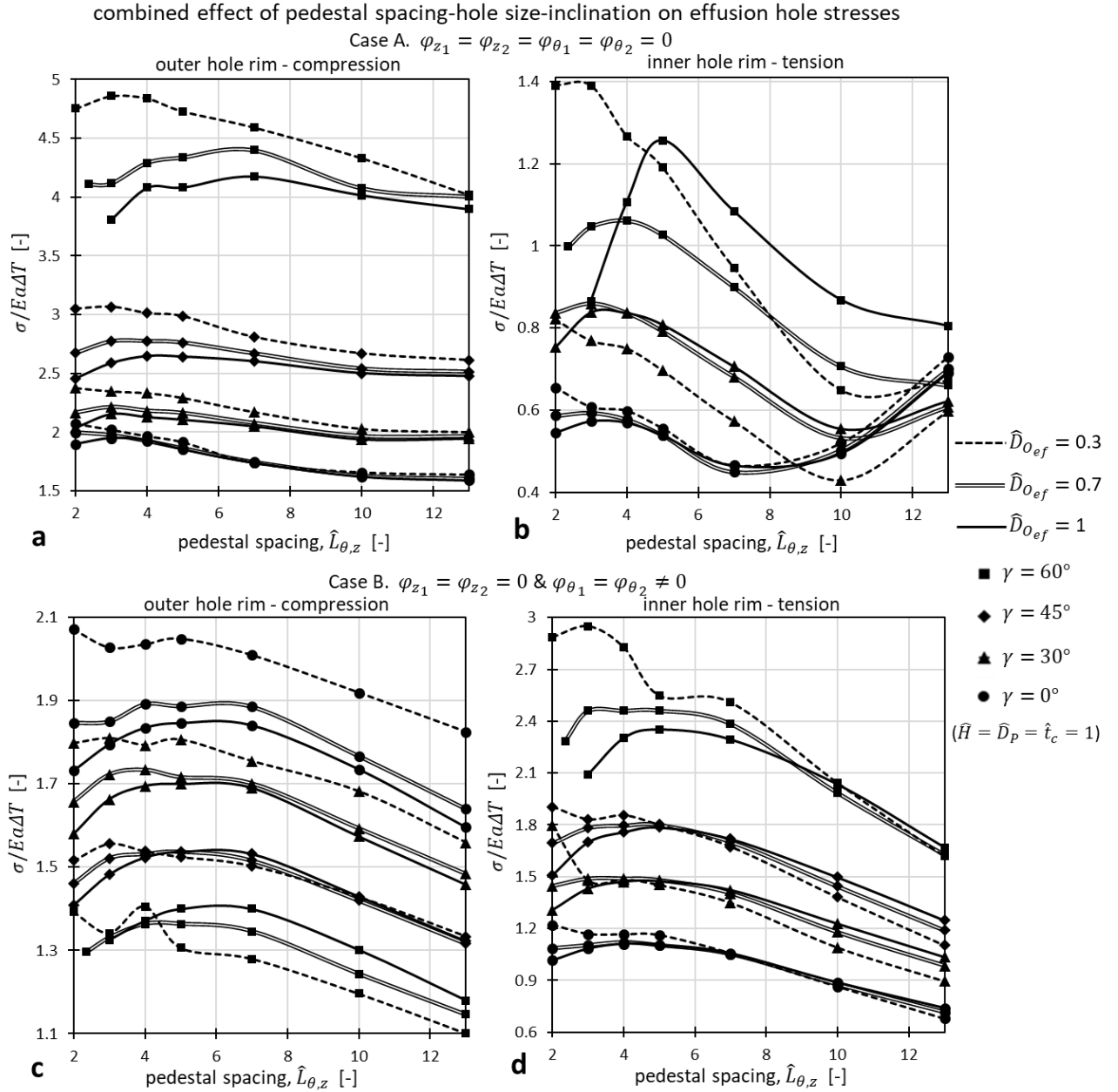


Figure 12. Peak stresses in the presence of holes (using FE model in Fig 2c). Fixed geometric ratios include: $\hat{R} = 20$, $\hat{t}_c = \bar{H} = \bar{D}_P = 1, \hat{p}_{Pf} = 0.1, \hat{p}_{Oef} = \hat{p}_{Oimp} = 0.05$. Plots (a-b) show the combined effect of pedestal spacing, $\hat{L}_{\theta,z}$, effusion hole size, \hat{D}_{Oef} , and effusion hole inclination, γ , on peak compressive (a) and peak tensile (b) stresses at the effusion hole for constraint case A; plots (c-d) show the corresponding results for constraint case B.

large holes, $\hat{D}_{Oef} = 0.7, 1$, the role of $\hat{L}_{\theta,z}$ in Figs 12a-d can be separated into two regimes; the regime, $\hat{L}_{\theta,z} > 5$, where hole stresses reduce with $\hat{L}_{\theta,z}$, and the $\hat{L}_{\theta,z} < 5$ regime where hole stresses increase with $\hat{L}_{\theta,z}$. Both the direct and indirect calculations of the max SCF in Figs 13a-h' show that the SCF increases (except for Figs 13b,d,f as explained above) with $\hat{L}_{\theta,z}$, while the agreement between the two calculations is improved for $\hat{L}_{\theta,z} > 5$. This is strong evidence that the interaction vanishes for large pedestal spacing, $\hat{L}_{\theta,z} > 5$. Figs 14a-d provides further evidence, in that for both cases A-B the influence of the hole on stresses at neighbouring pedestal outer fillets (at $\bar{\theta} = 1, \bar{z} = 0$, and at $\bar{\theta} = 0, \bar{z} = 1$ locations – denoted in Fig 2c) diminishes for $\hat{L}_{\theta,z} > 5$. In contrast, reducing $\hat{L}_{\theta,z}$ when $\hat{L}_{\theta,z} < 5$ is shown (Figs 13a-h') to reduce sharply the SCF based on the direct calculation, implying that the interaction effects are at play; for $\hat{L}_{\theta,z} < 5$, Figs 14a-d consistently indicate that the presence of the hole has a noticeable impact on stresses at the neighbouring pedestal outer fillets

(at $\bar{\theta} = 1, \bar{z} = 0$, and at $\bar{\theta} = 0, \bar{z} = 1$ – denoted in Fig 2c). For $\hat{L}_{\theta,z} = 2$, $\hat{D}_{Oef} = 1$, the direct SCF calculation is typically 25% lower than the indirect (conservative) hole-plate SCF solution throughout Figs 13a-h', with the difference being more pronounced for the large \hat{D}_{Oef} .

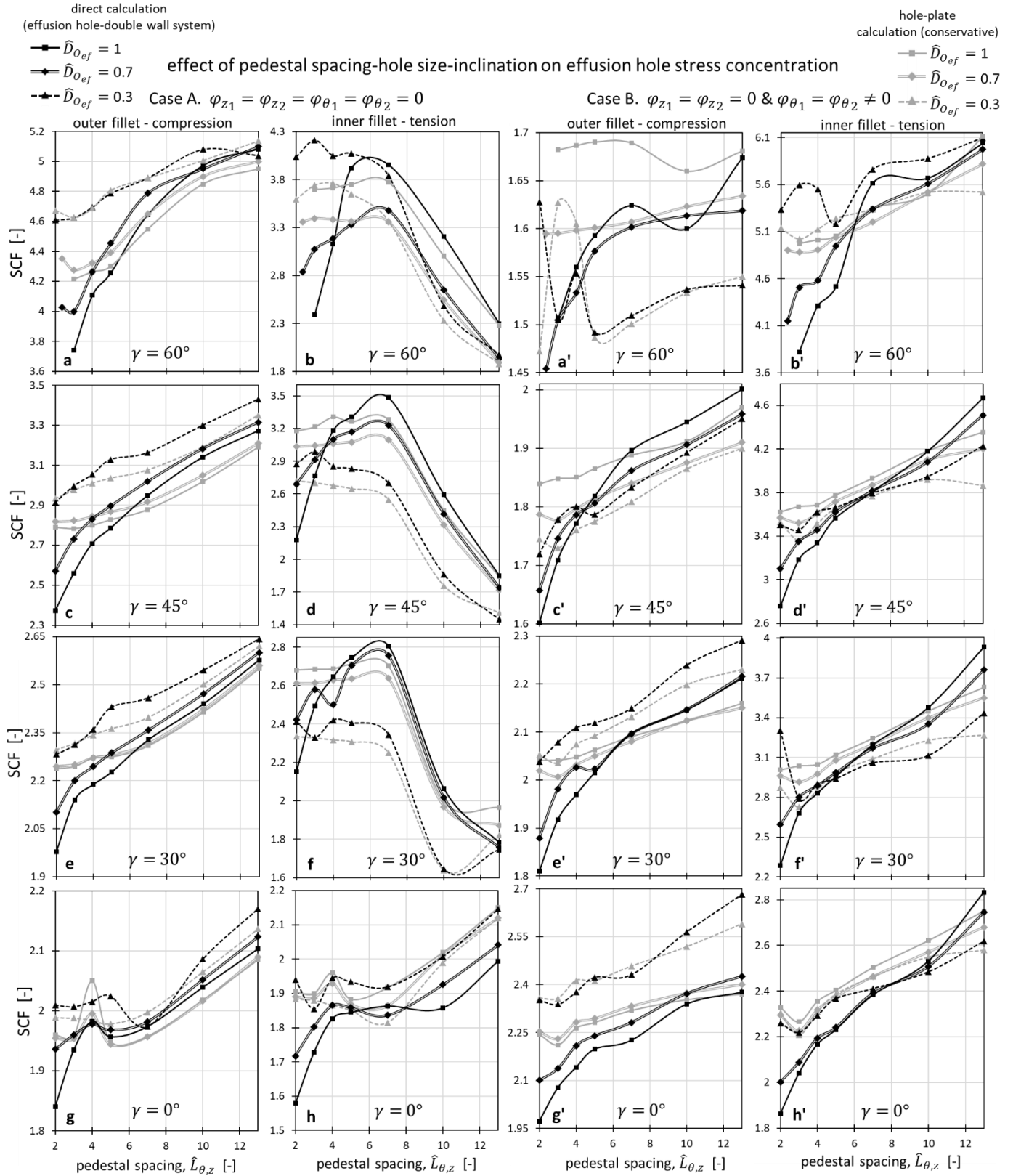


Figure 13. Direct and indirect (conservative) calculations of stress concentration factor (SCF) for the effusion hole stresses plotted in Figs 12a-d. Fixed geometric ratios include: $\hat{R} = 20$, $\hat{t}_c = \hat{H} = \hat{D}_p = 1$, $\hat{p}_{Pf} = 0.1$, $\hat{p}_{Oef} = \hat{p}_{imp} = 0.05$. For constraint case A, plots (a-h) show the direct (FE model in Fig 2c) and indirect (hole-plate FE model in Fig 2b) SCF calculations for different combinations of pedestal spacing, $\hat{L}_{\theta,z}$, effusion hole size, \hat{D}_{Oef} , and effusion hole inclination, γ . Plots (a'-h') show the corresponding SCF calculations for constraint case B.

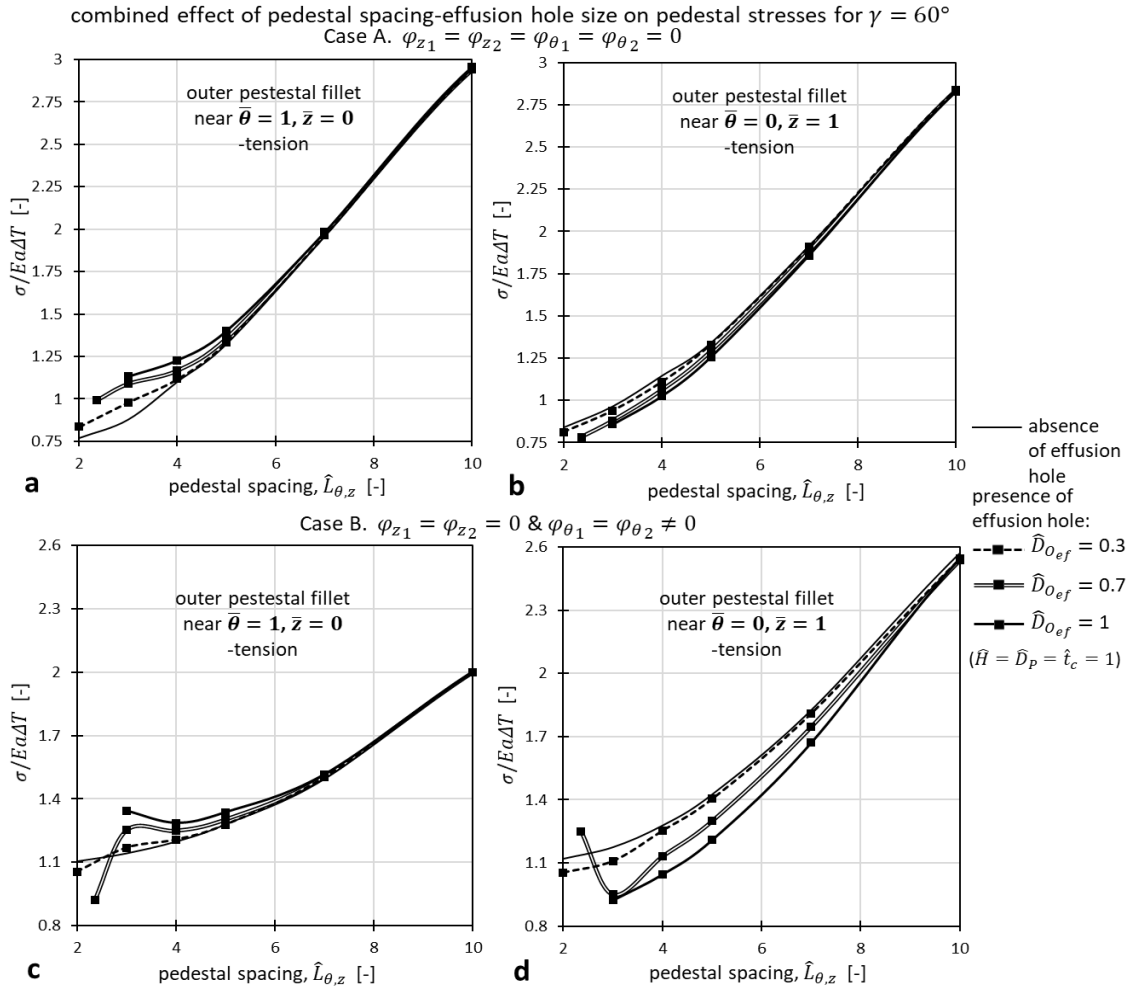


Figure 14. Illustration of tensile stresses in pedestals closest to the effusion hole (using FE model in Fig 2c). Fixed geometric ratios include: $\hat{R} = 20$, $\hat{t}_c = \hat{H} = \hat{D}_p = 1$, $\hat{\rho}_{pf} = 0.1$, $\hat{\rho}_{O_{ef}} = \hat{\rho}_{O_{imp}} = 0.05$ and $\gamma = 60^\circ$. For constraint case A, plots (a-b) show tensile stresses at the pedestal outer fillets corresponding to the positions $\bar{\theta} = 1, \bar{z} = 0$, and at $\bar{\theta} = 0, \bar{z} = 1$ (denoted in Fig 2c), as a function of pedestal spacing, $\hat{L}_{\theta,z}$, for different effusion hole sizes, $\hat{D}_{O_{ef}}$. Plots (c-d) provide the corresponding results for case B.

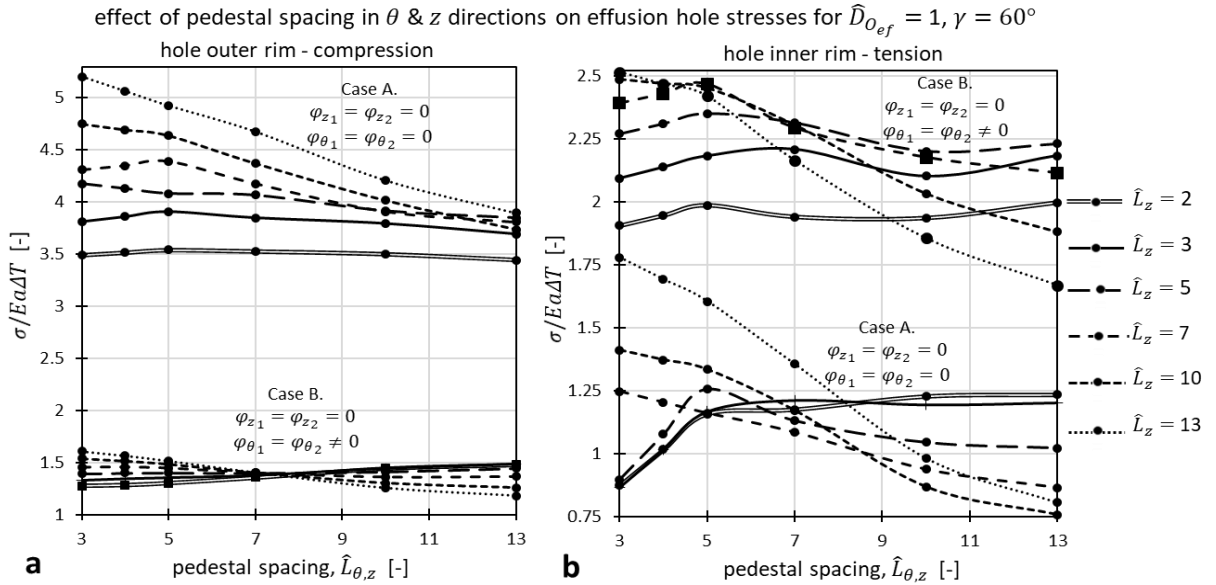


Figure 15. Sensitivity of effusion hole peak stresses with respect to pedestal spacing in θ and z directions (using FE model in Fig 2c). Fixed geometric ratios include: $\hat{R} = 20$, $\hat{t}_c = \hat{H} = \hat{D}_p = 1$, $\hat{\rho}_{pf} = 0.1$, $\hat{\rho}_{O_{ef}} = \hat{\rho}_{O_{imp}} = 0.05$ and $\hat{D}_{O_{ef}} = \hat{D}_{O_{imp}} = 1$, $\gamma = 60^\circ$. For constraint cases A-B, plot (a) shows peak compressive effusion hole stresses for different combinations of pedestal spacing, \hat{L}_θ , in the θ direction, and spacing \hat{L}_z , in the z direction. The corresponding peak tensile effusion hole stresses are plotted in (b).

Discrepancies between the two SCF calculations when the hole and pedestal do not interact, e.g. when $\hat{L}_{\theta,z} = 13$, are smaller than 6% in Figs 13a-h'. The error in the hole-plate SCF solution could relate to additional effects of curvature, which are not captured by the flat plate-hole FE model (Fig 2b), as well as by the fact that in an actual DWTC system the (nominal) bending moments and membrane forces vary with distance from the hole.

The purpose of Figs 13a-h' is to verify that the hole stresses for $\hat{L}_{\theta,z} > 5$ shown in Figs 12a-d, are determined by the fact that nominal stresses reduce with $\hat{L}_{\theta,z}$. The SCF calculations of Figs 13a-h' are used to indicate that the response for $\hat{L}_{\theta,z} < 5$ in Figs 12a-d is dictated by the decrease of SCF due to the hole-hole and hole-pedestal interactions as well as, potentially, by the decrease of stresses due to the increased porosity in the system; the synergy of these two effects dominate over the opposing effect of increasing nominal stresses at the hole for lower $\hat{L}_{\theta,z}$, in the regime $\hat{L}_{\theta,z} < 5$.

An additional effect shown in Figs 15a-b for $\hat{D}_{O_{ef}} = 1$, and $\gamma = 60^\circ$, is that the peak compressive and tensile stresses at the hole increase when pedestal spacing is large in one direction and simultaneously small in the perpendicular direction, i.e. $\hat{L}_\theta > 5$ and $\hat{L}_z < 5$, or $\hat{L}_z > 5$ and $\hat{L}_\theta < 5$. This is consistent with nominal stresses shown earlier in Figs 3c-d.

5.2.3 The general role of effusion hole size

From Figs 12a-d, it is evident that the onset of interaction and porosity effects occurs at larger $\hat{L}_{\theta,z}$ for larger inclination, γ , and hole size, $\hat{D}_{O_{ef}}$. Minimising $\hat{L}_{\theta,z}$ for the small hole, $\hat{D}_{O_{ef}} = 0.3$, leads to only a slight decrease in hole stresses. A weak interaction effect for small holes may be attributed not only to the smaller stress perturbation zone induced by the hole, but also to its lower proximity with respect to the perturbation around the pedestal. Noteworthy is that the centre of the inner rim of the holes is here consistently located in the middle of the pedestal spacing, $\hat{L}_{\theta,z}$, and as a result, for a given $\hat{L}_{\theta,z}$ the location of the peak tensile stress at a smaller hole is further from the neighbouring pedestal compared to a large hole; as a result the small hole gives larger tensile stress (see Figs 11e-f). The opposite occurs in terms of the proximity of outer hole rim (peak compressive stress) to the nearest pedestal axis; again, here, smaller holes exhibit higher stresses (see Fig 11e-f) since the nominal stresses at the hot surface near the pedestals i.e. at $\bar{\theta} = 1, \bar{z} = 0$, are higher than at the location away from pedestals i.e. at $\bar{\theta} = \bar{z} = 0$ (shown earlier in Figs 3a-d).

The small hole size, $\hat{D}_{O_{ef}} = 0.3$, however, allows for locating the hole in closer proximity to the neighbouring pedestals, as well as for using even narrower pedestal spacing below the minimum value, $\hat{L}_{\theta,z} = 2$ in Figs 12a. A $\hat{L}_{\theta,z} < 2$ for the current design (Figs 12a-d), however, would imply an extremely narrow spacing between the pedestals intersecting with the plane $\zeta = 0$ in Fig 2c, suggesting that thinner pedestals should also be used. Such an optimisation will be considered in a later study.

5.2.4 The role of effusion hole size for closest hole-pedestal spacing

In this study, we focus on the contribution that arises solely from the hole size, $\hat{D}_{O_{ef}}$. We fix $\hat{L}_{\theta,z} = 3$ and $\gamma = 60^\circ$, and place the effusion hole as close as possible to the pedestal in the θ direction (as for example occurs in Figs 11e,g). Figs 16a-c display maximum absolute principal stresses, $\sigma = \max(|\sigma_1|, |\sigma_2|, |\sigma_3|)$, normalised by $Ea\Delta T$, for the extreme cases of $\hat{D}_{O_{ef}} = 0.25, \hat{D}_P = 1.5$ (Fig 16a) and $\hat{D}_{O_{ef}} = 1.2, \hat{D}_P = 0.5$ (Fig 16c), along with the more reasonable combination $\hat{D}_{O_{ef}} = 0.8, \hat{D}_P = 1$ (Fig 16b), while the peak hole stresses and adjacent pedestal fillet are plotted in Fig 16d and Fig 16e, respectively.

effect of size ratio between effusion hole-pedestal
on corresponding stresses for $\gamma = 60^\circ$

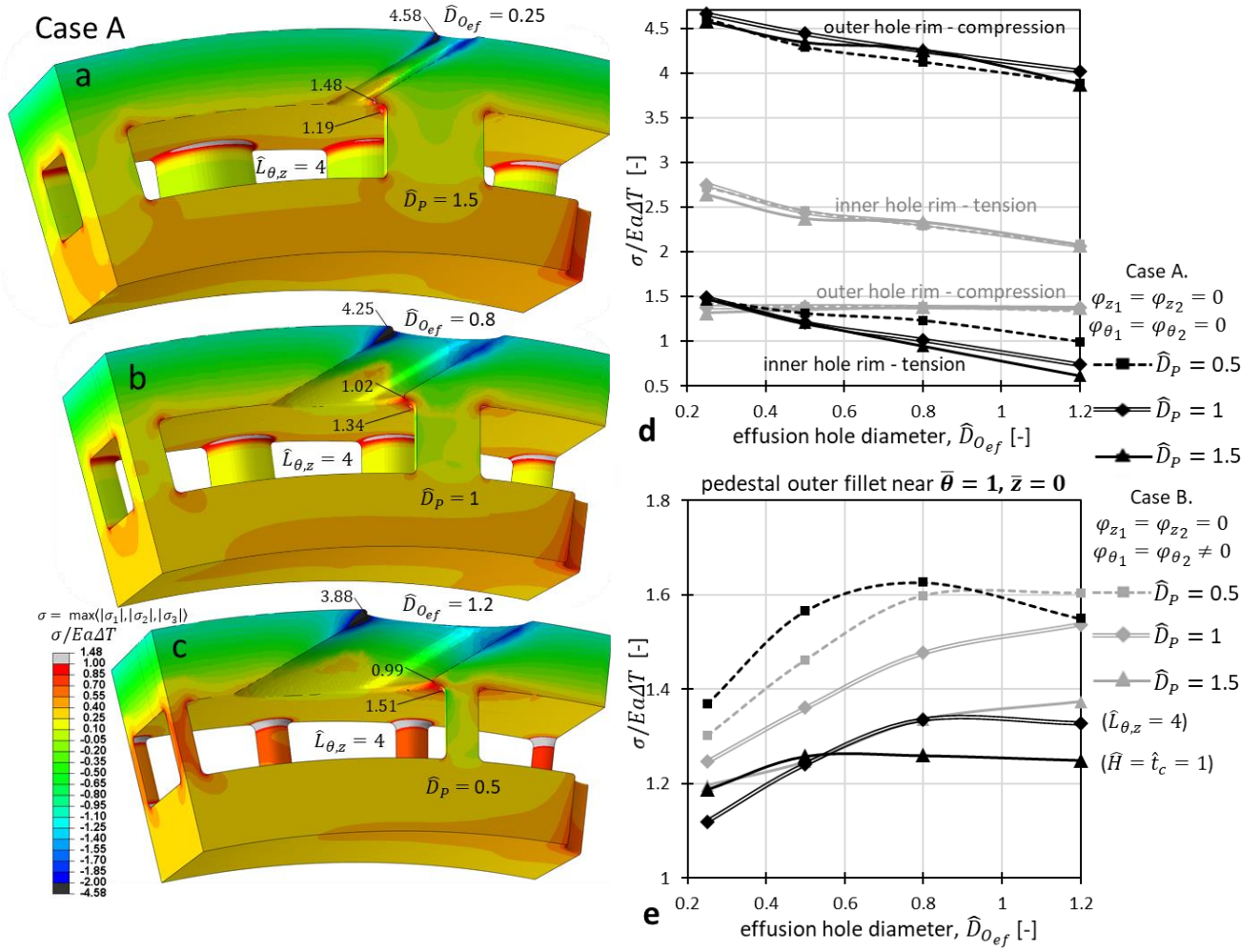


Figure 16. Sensitivity of effusion hole peak stresses with respect to effusion hole-pedestal size ratio, for closest hole-pedestal spacing (using FE model in Fig 2c). Fixed geometric ratios include: $\hat{R} = 20$, $\hat{t}_c = \hat{H} = 1$, $\hat{\rho}_{Pf} = 0.1$, $\hat{\rho}_{O_{ef}} = \hat{\rho}_{O_{imp}} = 0.05$ and $\hat{D}_{O_{imp}} = 1$, $\gamma = 60^\circ$. For constraint case A, images (a-c) show FE maximum principal stress contours for three combinations of effusion hole diameter, $\hat{D}_{O_{ef}}$, and pedestal diameter, \hat{D}_p . For both cases A-B, plot (d) shows the sensitivity of peak compressive and tensile stresses at the effusion hole with respect to $\hat{D}_{O_{ef}}$, for different \hat{D}_p values. The corresponding tensile stresses at the pedestal fillet near the effusion hole (at $\bar{\theta} = 1, \bar{z} = 0$) are plotted in (e).

By comparing Fig 16d with Figs 12a-d for $\hat{L}_{\theta,z} = 3$ and $\gamma = 60^\circ$, we conclude that fixing $\hat{L}_{\theta,z}$ and locating the hole near the pedestal (at $\bar{\theta} = 1, \bar{z} = 0$ – see Fig 3a) leads to a slight increase in peak stresses compared to the case when the inner rim of the hole is located midway between the pedestals (Figs 12a-d); the effect becomes less profound with increasing $\hat{D}_{O_{ef}}$. Nevertheless, the above trend is specific to $\hat{L}_{\theta,z} = 3$ (and $\gamma = 60^\circ$) and may change for different $\hat{L}_{\theta,z}$ (and γ). More importantly, Figs 16a-e shows that hole stresses reduce with hole size, $\hat{D}_{O_{ef}}$, and practically are not affected by pedestal size, \hat{D}_p . This reveals that the size of the stress perturbation zone induced by the hole along with the potential effect of porosity dominate.

Noteworthy is that so far we have considered realistic, fixed values of fillet radii for the hole rim, $\hat{\rho}_{O_{ef}} = 0.05$ (denoted in Fig 2c), and pedestal, $\hat{\rho}_{Pf} = 0.1$ (denoted in Fig 2a). For the minimum hole-pedestal spacing considered here, the interaction effect may show a degree of sensitivity to $\hat{\rho}_{O_{ef}}, \hat{\rho}_{Pf}$. Independently, $\hat{\rho}_{O_{ef}}$, may influence the max SCF values reported in Figs 12-13, and this is explored in the final next section.

5.3 Effect of hole fillets

We obtain independent SCF results using the hole-plate model in Fig 2b. For the transverse circular hole, Figs 17a-b show the effect of fillet radius and plate thickness ratio, ρ_{of}/t , on the percentage change in max SCF with respect to $\rho_{of}/t = 0$ i.e. no fillet. For the equibiaxial state, $\sigma_x/\sigma_y = 1$, the max SCF reduces with ρ_{of}/t in bending but increases in tension (see Fig 17a). For equal tension-bending i.e. $\% \bar{\sigma}/\sigma = 50$, the SFC lies between the extremes of pure tension and pure bending and decreases with ρ_{of}/t (Fig 17a). For $\sigma_2/\sigma_1 = 0$ (see Fig 17b) the behaviour is more complex and depends on D_{oy}/t for pure bending while in pure bending ρ_{of}/t has a weak effect on SCF. Varying D_{oy}/t requires caution, since different ρ_{of}/t implies different D_{oy}/ρ_{of} , introducing additional effects; the role of the additional length-scale, D_{oy}/ρ_{of} , is not investigated here. Theoretically, the stress gradient in the vicinity of the hole rim is expected to be smoother for higher ρ_{of}/t (decreasing max SCF), although this reduces the plate thickness locally (increasing max SCF). Sensibly, for pure bending the positive effect of ρ_{of}/t dominates (Fig 17a), whereas tension gives rise to the negative effect, in consistency with previous reports [64].

These positive and negative effects of ρ_{of}/t , corresponding to pure bending and pure tension continue to apply for inclined holes with elliptical rims in both equibiaxial, $\sigma_x/\sigma_y = 1$ (see Figs 17c), and uniaxial, $\sigma_x/\sigma_y = 0$, (see Figs 17d) loading. The difference is that ρ_{of}/t reduces the max SCF at the 90° wedge in both pure tension and pure bending when $\sigma_y/\sigma_x = 0$; these results for pure tension are consistent with experimental data reported in [41, 42, 64].

Based on the above results for the fundamental hole-plate problem (Figs 17a-e), we now interpret the effect of hole fillet radius, $\hat{\rho}_{of}$, within the DWTC system (FE model in Fig 2c), for fixed $\hat{L}_{\theta,z} = 4$ and $\gamma = 60^\circ$. For case A, Fig 17f shows that reducing \hat{D}_{of} , whilst increasing $\hat{\rho}_{of}$, increases the SCF at the acute wedge-elliptical vertex of the outer hole rim. The larger increase of SCF for $\hat{D}_{of} = 0.3$ (Fig 17f) relates to the fact that increasing $\hat{\rho}_{of}$ in a small hole also decreases $\hat{D}_{of}/\hat{\rho}_{of}$, as suggested in [34]. The overall increase of SCF with $\hat{\rho}_{of}$ in the outer hole rim (Fig 17f) owes to the membrane force contribution, $\% \bar{\sigma}/\sigma \approx 35$ (shown earlier in Figs 4a) at this location, in consistency with the SCF behaviour for pure tension shown in Fig 17c. In contrast, the overall decrease of SCF with $\hat{\rho}_{of}$ in the tensile inner rim relates to the largely negative membrane force contribution, $\% \bar{\sigma}/\sigma \approx -100$ (shown earlier in Figs 4b). Similarly, for case B in Fig 17g, the overall decrease of SCF with $\hat{\rho}_{of}$ is explained by the smaller contribution of tension and the dominance of bending compared to case A (described earlier in Figs 4c-d).

Figs 17f-g, demonstrate that combining the thermal stress solutions in the absence of holes with independent hole-plate results is a powerful strategy for interpreting complex effects of effusion hole fillet radius on the peak hole stresses. We conclude that increasing $\hat{\rho}_{of}$ requires caution, as it does not always reduce the max SCF. Increasing the hole fillet size up to $\hat{\rho}_{of} = 0.05$ offers SCF reductions of the order of 15%.

6 Conclusions

We have evaluated how oblique effusion holes influence the stress state in double wall transpiration cooling (DWTC) systems. These systems will allow components to be exposed to extreme temperatures in order to gain efficiency in gas turbine and hypersonic flight applications. Our results provide the essential information required for the design and commercial implementation of such cooling systems.

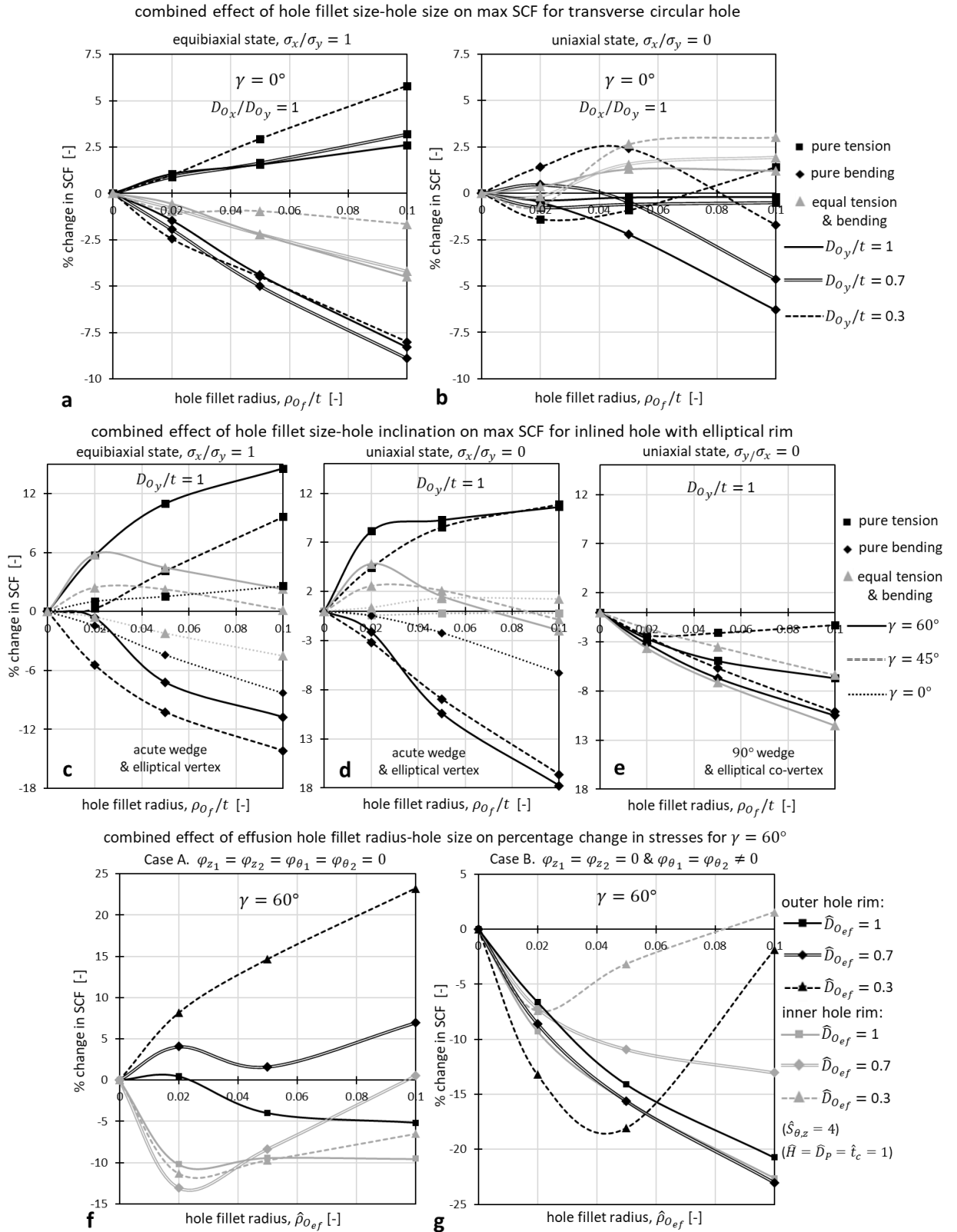


Figure 17. Effect of hole fillet radius on the maximum hole stress concentration factor (SCF). (a-b) Transverse circular holes (using the hole-plate FE model in 2b) - plots show the effect of the normalised hole fillet radius, ρ_{0f}/t , on the percentage change in maximum SCF, under pure tension, pure bending and equal tension and bending, for different hole size ratios, D_{0y}/t ; plots (a) and (b) correspond to equibiaxial, $\sigma_x/\sigma_y = 1$, and uniaxial, $\sigma_x/\sigma_y = 0$, stress states respectively. (c-e) The corresponding results for inclined holes with elliptical rims (using the hole-plate FE model in 2b) for fixed hole size, $D_{0y}/t = 1$, and varying inclination, γ ; plots (c) and (d) correspond to equibiaxial, $\sigma_x/\sigma_y = 1$, and uniaxial, $\sigma_x/\sigma_y = 0$, stress states respectively, and refer to the acute wedge-elliptical vertex region, whereas plot (e) refers to the 90° wedge-elliptical co-vertex region under uniaxial states, $\sigma_y/\sigma_x = 0$. (f-g) Effusion hole SCFs in the double wall system (using FE model in Fig 2c), for cases A-B, showing the effect of fillet radius, $\hat{\rho}_{0ef}$, on the percentage change in maximum SCF at the outer, hot, compressive hole rim and the inner, cool, tensile hole rim, for different effusion hole size ratios, \hat{D}_{0ef} . Fixed geometric ratios here include: $\hat{R} = 20$, $\hat{L}_{\theta,z} = 4$, $\hat{t}_c = \hat{H} = \hat{D}_p = \hat{D}_{0imp} = 1$, $\hat{\rho}_{Pf} = 0.1$, $\hat{\rho}_{0imp} = 0.05$ and $\gamma = 60^\circ$.

A temperature gradient across the hot outer wall is shown to induce in-plane membrane forces and bending moments in the system, such that effusion holes undergo peak compressive stresses at the outer hot rim and peak tensile stresses at the inner cooler rim. The compressive effusion hole stresses are much more severe than stresses in the wall connecting pedestals and in impingement holes and their large magnitude suggests that significant local creep-fatigue processes occur, leading to low cycle fatigue failure.

Effusion hole stresses result from the superposition of the nominal thermal stresses in the absence of holes, the stress concentration factor (SCF) for an isolated effusion hole in a large plate, the decrease of SCF due to hole-hole and hole-pedestal interactions, and a potential overall reduction of structural stiffness at high porosities. The study demonstrates that critical hole stresses can be effectively reduced via decreasing the corresponding nominal stresses. Decreasing the density of the connecting pedestals decreases nominal thermal stresses at the effusion hole location, whereas maximising the density enhances the interaction and porosity effects, which can lead to reductions of 25% in effusion hole stresses. The effect of pedestal height (or wall spacing) arises only when the two walls are allowed to rotate.

Large effusion hole inclinations of $\gamma = 60^\circ$ to the surface normal, can lead to extreme values of $SCF = 5$ and these are relieved by 40% when using $\gamma = 45^\circ$. An opportunity for using $\gamma = 60^\circ$, yet, with the enormous benefit of a 50% reduced SCF, arises by eliminating the ellipticity of the conventional oblique, effusion hole profile where it cuts the plane of the inner and outer surfaces. This is not possible with standard hole drilling techniques, but is achievable using a range of evolving technologies, such as additive manufacturing.

Our thermoelastic FE data provide the key input parameters for creep-fatigue life calculation schemes, i.e. local strain approach [65, 66], that account for localised plasticity and creep at holes, using techniques such as those proposed by Neuber [52]. Our results allow the potential design space to be reduced by providing a limited range of potential configurations to use in more detailed FE analysis in the creep-plasticity range, under realistic thermomechanical loading cycling.

Acknowledgements

The authors acknowledge Dr Alex Murray for providing useful feedback on this study. This research was supported by EPSRC Programme Grant EP/P000878/1.

REFERENCES

1. Singh, H., A. Ye, and M.J. Ferrua, *Aspects of food structures in the digestive tract*. Current Opinion in Food Science, 2015. 3: p. 85-93.
2. Broomfield, R.W., et al., *Development and turbine engine performance of three advanced rhenium containing superalloys for single crystal and directionally solidified blades and vanes*. 1998.
3. Krewinkel, R., *A review of gas turbine effusion cooling studies*. International Journal of Heat and Mass Transfer, 2013. 66: p. 706-722.
4. Cerminara, A., R. Deiterding, and N.D. Sandham, *Transpiration cooling using porous material for hypersonic applications*. Convective Heat Transfer in Porous Media, 2019: p. 263.
5. Ngetich, G.C., et al., *A three-dimensional conjugate approach for analyzing a double-walled effusion-cooled turbine blade*. Journal of Turbomachinery, 2019. 141(1).
6. Reed, R.C., *The superalloys: fundamentals and applications*. 2008: Cambridge university press.
7. Sweeney, P.C. and J.F. Rhodes, *An infrared technique for evaluating turbine airfoil cooling designs*. J. Turbomach., 2000. 122(1): p. 170-177.
8. Hermann, T.A., I. Naved, and M. McGilvray. *Performance of Transpiration Cooled Heat Shields for Hypersonic Vehicles*. in *AIAA Scitech 2019 Forum*. 2019.

9. Murray, A.V., *Advanced gas turbine cooling: double-wall turbine cooling technologies in turbine NGV/blade applications*. 2019, University of Oxford.
10. Baheri, S., S.A. Tabrizi, and B. Jubran, *Film cooling effectiveness from trenched shaped and compound holes*. *Heat and mass transfer*, 2008. 44(8): p. 989-998.
11. Wang, C., J. Zhang, and J. Zhou, *Optimization of a fan-shaped hole to improve film cooling performance by RBF neural network and genetic algorithm*. *Aerospace Science and Technology*, 2016. 58: p. 18-25.
12. Han, J.-C., S. Dutta, and S. Ekkad, *Gas turbine heat transfer and cooling technology*. 2012: CRC press.
13. Funazaki, K., et al. *Heat Transfer Characteristics of an Integrated Cooling Configuration for Ultra-High Temperature Turbine Blades: Experimental and Numerical Investigations*. in *ASME Turbo Expo 2001: Power for Land, Sea, and Air*. 2001. American Society of Mechanical Engineers Digital Collection.
14. Murray, A.V., P.T. Ireland, and A.J. Rawlinson. *An Integrated Conjugate Computational Approach for Evaluating the Aerothermal and Thermomechanical Performance of Double-Wall Effusion Cooled Systems*. in *ASME Turbo Expo 2017: Turbomachinery Technical Conference and Exposition*. 2017. American Society of Mechanical Engineers Digital Collection.
15. Elmukashfi, E., et al., *Analysis of the Thermomechanical Stresses in Double-Wall Effusion Cooled Systems*. *Journal of Turbomachinery*, 2020. 142(5).
16. Padture, N.P., M. Gell, and E.H. Jordan, *Thermal barrier coatings for gas-turbine engine applications*. *Science*, 2002. 296(5566): p. 280-284.
17. Kim, K.M., et al., *Optimal design of impinging jets in an impingement/effusion cooling system*. *Energy*, 2014. 66: p. 839-848.
18. Cerri, G., et al., *Advances in effusive cooling techniques of gas turbines*. *Applied Thermal Engineering*, 2007. 27(4): p. 692-698.
19. Zhou, Z., et al., *Effect of skew angle of holes on the tensile behavior of a Ni-base single crystal superalloy*. *Journal of Alloys and Compounds*, 2015. 628: p. 158-163.
20. Zhou, Z.-J., et al., *Effect of skew angle of holes on the thermal fatigue behavior of a Ni-based single crystal superalloy*. *Acta Metallurgica Sinica (English Letters)*, 2017. 30(2): p. 185-192.
21. Gemma, A. and J. Phillips, *The application of fracture mechanics to life prediction of cooling hole configurations in thermal-mechanical fatigue*. *Engineering Fracture Mechanics*, 1977. 9(1): p. 25-36.
22. Wen, Z., et al., *A combined CP theory and TCD for predicting fatigue lifetime in single-crystal superalloy plates with film cooling holes*. *International Journal of Fatigue*, 2018. 111: p. 243-255.
23. Sadowski, T. and P. Golewski, *Detection and numerical analysis of the most efforted places in turbine blades under real working conditions*. *Computational Materials Science*, 2012. 64: p. 285-288.
24. Rauch, M. and E. Roos, *Life assessment of multiaxially cyclic loaded turbine components*. *Fatigue & Fracture of Engineering Materials & Structures*, 2008. 31(6): p. 441-451.
25. Chen, L.J., Y.H. Liu, and L.Y. Xie, *Power-exponent function model for low-cycle fatigue life prediction and its applications - Part II: Life prediction of turbine blades under creep-fatigue interaction*. *International Journal of Fatigue*, 2007. 29(1): p. 10-19.
26. Tang, W., et al., *Numerical simulation of temperature distribution and thermal-stress field in a turbine blade with multilayer-structure TBCs by a fluid-solid coupling method*. *Journal of Materials Science & Technology*, 2016. 32(5): p. 452-458.
27. Skamniotis, C. and A.C. Cocks, *Minimising thermal stresses in double wall transpiration cooled components for high temperature applications*. *International Journal of Mechanical Sciences*, 2020: p. 105983.
28. Skamniotis, C.G. and A.C. Cocks, *2D and 3D thermoelastic phenomena in double wall transpiration cooling systems for gas turbine blades and hypersonic flight*. *Aerospace Science and Technology*, 2021: p. 106610.
29. Yang, Z., et al., *The concentration of stress and strain in finite thickness elastic plate containing a circular hole*. *International Journal of Solids and Structures*, 2008. 45(3-4): p. 713-731.
30. Li, Z., W. Guo, and Z. Kuang, *Three-dimensional elastic stress fields near notches in finite thickness plates*. *International Journal of Solids and Structures*, 2000. 37(51): p. 7617-7632.
31. Yang, Z., *The stress and strain concentrations of an elliptical hole in an elastic plate of finite thickness subjected to tensile stress*. *International journal of fracture*, 2009. 155(1): p. 43.
32. Guo, W. and W. Guo, *Formulization of Three-Dimensional Stress and Strain Fields at Elliptical Holes in Finite Thickness Plates*. *Acta Mechanica Solida Sinica*, 2019. 32(4): p. 393-430.

33. She, C. and W. Guo, *Three-dimensional stress concentrations at elliptic holes in elastic isotropic plates subjected to tensile stress*. International Journal of Fatigue, 2007. 29(2): p. 330-335.
34. Pilkey, W.D., D.F. Pilkey, and Z. Bi, *Peterson's stress concentration factors*. 2020: John Wiley & Sons.
35. Stanley, P. and B. Day, *Stress concentrations at an oblique hole in a thick flat plate under an arbitrary in-plane biaxial loading*. The Journal of Strain Analysis for Engineering Design, 1993. 28(3): p. 223-235.
36. Stanley, P. and A. Starr, *Stress concentrations at an oblique hole in a thick plate*. The Journal of Strain Analysis for Engineering Design, 2000. 35(2): p. 143-147.
37. Nihous, G.C., C.K. Kinoshita, and S.M. Masutani, *Stress concentration factors for oblique holes in pressurized thick-walled cylinders*. Journal of pressure vessel technology, 2008. 130(2).
38. Grover, S.M., *Computational Study of Stress Concentration About an Oblique Hole in a Thick Walled Tube: Toward Understanding Structural Improvements in Bone*. 2004, University of Florida.
39. Dulieu-Barton, J. and S. Quinn, *Thermoelastic stress analysis of oblique holes in flat plates*. International journal of mechanical sciences, 1999. 41(4-5): p. 527-546.
40. Ellyin, F., *Experimental study of oblique circular cylindrical apertures in plates*. Experimental Mechanics, 1970. 10(5): p. 195-202.
41. Daniel, I.M., *Photoelastic analysis of stresses around oblique holes*. Experimental Mechanics, 1970. 10(11): p. 467-473.
42. Ellyin, F. and U. Izmiroglu, *Effect of corner shape on elastic stress and strain concentration in plates with an oblique hole*. 1973.
43. Li, W., et al., *Large eddy simulation of compound angle hole film cooling with hole length-to-diameter ratio and internal crossflow orientation effects*. International Journal of Thermal Sciences, 2017. 121: p. 410-423.
44. Zhang, H., et al., *Effects of compound angle on film cooling effectiveness considering endwall lateral pressure gradient*. Aerospace Science and Technology, 2020: p. 105923.
45. Körner, C., et al., *Microstructure and mechanical properties of CMSX-4 single crystals prepared by additive manufacturing*. Metallurgical and Materials Transactions A, 2018. 49(9): p. 3781-3792.
46. Ponter, A. and S. Karadeniz, *An extended shakedown theory for structures that suffer cyclic thermal loading, Part 1: Theory*. 1985.
47. Karadeniz, S. and A. Ponter, *The influence of transient thermal loading on the Bree plate; A simplified method of analysis*. Nuclear Engineering and Design, 1984. 80(3): p. 359-374.
48. Karadeniz, S., A. Ponter, and K. Carter, *The plastic ratcheting of thin cylindrical shells subjected to axisymmetric thermal and mechanical loading*. 1987.
49. Chen, H. and A.R. Ponter, *Shakedown and limit analyses for 3-D structures using the linear matching method*. International Journal of Pressure Vessels and Piping, 2001. 78(6): p. 443-451.
50. Ma, Z., et al., *A unified direct method for ratchet and fatigue analysis of structures subjected to arbitrary cyclic thermal-mechanical load histories*. International Journal of Mechanical Sciences, 2021. 194: p. 106190.
51. Mücke, R. and O.-E. Bernhardt, *A constitutive model for anisotropic materials based on Neuber's rule*. Computer methods in applied mechanics and engineering, 2003. 192(37-38): p. 4237-4255.
52. Neuber, H., *Theory of stress concentration for shear-strained prismatical bodies with arbitrary nonlinear stress-strain law*. 1961.
53. Ince, A., G. Glinka, and A. Buczynski, *Computational modeling of multiaxial elasto-plastic stress-strain response for notched components under non-proportional loading*. International Journal of Fatigue, 2014. 62: p. 42-52.
54. Li, Z., et al., *Deformation and recrystallization of single crystal nickel-based superalloys during investment casting*. Journal of Materials Processing Technology, 2015. 217: p. 1-12.
55. Wen, Z., et al., *Equivalent and simplification of nickel-based single crystal plates with film cooling holes*. Aerospace Science and Technology, 2018. 82: p. 119-139.
56. Dye, D., et al. *Welding of Single Crystal Superalloy CMSX-4: Experiments and Modeling*. in *Superalloys 2004 (Tenth International Symposium)*. 2004.
57. Wang, J., et al., *The inter-hole interference on creep deformation behavior of nickel-based single crystal specimen with film-cooling holes*. International Journal of Mechanical Sciences, 2019. 163: p. 105090.
58. Hou, N., et al., *The influence of crystal orientations on fatigue life of single crystal cooled turbine blade*. Materials Science and Engineering: A, 2008. 492(1-2): p. 413-418.
59. Murray, A.V., P.T. Ireland, and E.J.J.o.T. Romero, *Development of a Steady-State Experimental Facility for the Analysis of Double-Wall Effusion Cooling Geometries*. 2019. 141(4): p. 041008.

60. Murray, A., et al., *High Resolution Experimental and Computational Methods for Modelling Multiple Row Effusion Cooling Performance*. 2018. 3(1): p. 4.
61. Skamniotis, C. and A.C. Cocks, *Multiscale analysis of thermomechanical stresses in double wall transpiration cooling systems for gas turbine blades*. To appear, 2021.
62. Systèmes, D., *Abaqus*. Providence, RI: Dassault Systèmes.[Google Scholar], 2016.
63. Inglis, C.E., *Stresses in a plate due to the presence of cracks and sharp corners*. Trans Inst Naval Archit, 1913. 55: p. 219-241.
64. McKenzie, H. and D. White, *Stress concentration caused by an oblique round hole in a flat plate under uniaxial tension*. Journal of Strain Analysis, 1968. 3(2): p. 98-102.
65. Visvanatha, S., P. Straznicky, and R. Hewitt, *Influence of strain estimation methods on life predictions using the local strain approach*. International Journal of Fatigue, 2000. 22(8): p. 675-681.
66. Banaszekiewicz, M., *Numerical investigations of crack initiation in impulse steam turbine rotors subject to thermo-mechanical fatigue*. Applied Thermal Engineering, 2018. 138: p. 761-773.